
Analysis of the Equilibrium Phase in Immune-Controlled Tumors Provides Hints for Designing Better Strategies for Cancer Treatment

Kevin Atsou¹, Sokchea Khou^{2,#}, Fabienne Anjuère¹, Véronique M. Braud^{2,*} and Thierry Goudon^{1,*}

¹ *Université Côte d'Azur, Inria, CNRS, LJAD, Nice, France*

² *Université Côte d'Azur, CNRS, Institut de Pharmacologie Moléculaire et Cellulaire UMR 7275 Valbonne, France*

[#] *Current address: Department of Cell, Developmental & Cancer Biology, Oregon Health & Science University, Portland, USA*

Correspondence*:

These authors contributed equally to this work and share the last authorship

Véronique M. Braud
Université Côte d'Azur, CNRS, Institut de Pharmacologie Moléculaire et Cellulaire
UMR 7275 660 Route des Lucioles, F-06560 Valbonne, France
braud@ipmc.cnrs.fr

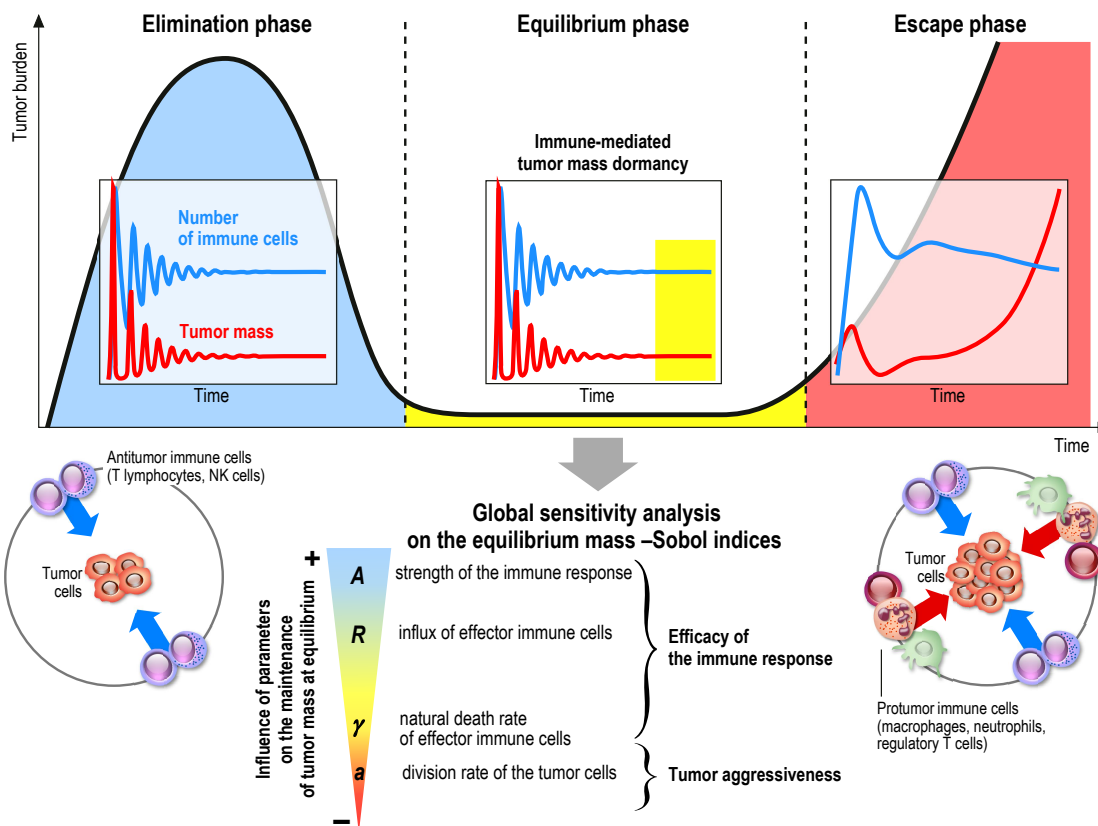
Thierry Goudon
Université Côte d'Azur, Inria, CNRS, LJAD, Parc Valrose, F-06108 Nice, France
thierry.goudon@inria.fr

2 ABSTRACT

3 When it comes to improving cancer therapies, one challenge is to identify key biological
4 parameters that prevent immune escape and maintain an equilibrium state characterized
5 by a stable subclinical tumor mass, controlled by the immune cells. Based on a space
6 and size structured partial differential equation model, we developed numerical methods
7 that allow us to predict the shape of the equilibrium at low cost, without running
8 simulations of the initial-boundary value problem. In turn, the computation of the
9 equilibrium state allowed us to apply global sensitivity analysis methods that assess
10 which and how parameters influence the residual tumor mass. This analysis reveals
11 that the elimination rate of tumor cells by immune cells far exceeds the influence of the
12 other parameters on the equilibrium size of the tumor. Moreover, combining parameters
13 that sustain and strengthen the antitumor immune response also proves more efficient
14 at maintaining the tumor in a long-lasting equilibrium state. Applied to the biological
15 parameters that define each type of cancer, such numerical investigations can provide
16 hints for the design and optimization of cancer treatments.

17 **Keywords:** cancer, mathematical oncology, equilibrium phase, immunotherapy, drug response

GRAPHICAL ABSTRACT



18

1 INTRODUCTION

19 The immune system plays a major role in the control of tumor growth. This has led to the
 20 concept of immune surveillance and cancer immunoediting composed of three phases (1, 2, 3):
 21 the elimination, when tumors are rapidly eradicated by the immune system, the equilibrium, a
 22 latency period when tumors can survive but remain on a controlled state, and the escape, the
 23 final outgrowth of tumors that have outstripped immunological restraints. In this later phase,
 24 immune suppression is prevailing and immune cells are also subverted to promote tumor growth.
 25 Numerous cancer immunotherapy strategies have been designed and assessed to counteract
 26 immune suppression and restore effective and durable elimination of tumors (4, 5, 6, 7, 8).
 27 They show improved efficacy over conventional anticancer treatments but only a minority of
 28 patients respond. The challenge to face now is to identify key biological parameters which will
 29 convert a fatal outcome into a chronic, manageable state, the durable maintenance of cancer in
 30 a viable equilibrium phase controlled by immunity. Reaching such immune-mediated tumor
 31 mass dormancy is indeed the first key step for successful control of tumor growth and a goal
 32 for immunotherapy (9). The equilibrium state is however difficult to apprehend experimentally
 33 because the tumor mass at equilibrium is below detectable limits (3). Mathematical modeling
 34 of the tumor-immune system interactions offers useful information about the features of the

35 equilibrium phase during primary tumor development, and such tools could be used to guide the
36 design of optimal anticancer therapies (10, 11, 12, 13).

37 We previously (10) introduced a specific multiscale mathematical model based on partial
38 differential equations (PDE), intended to describe the earliest stages of tumor-immune system
39 interactions. We conjecture that the space heterogeneities of the distribution of active and resting
40 immune cells, which are subjected to several interaction mechanisms with the tumor cells,
41 plays a critical role in the efficiency of the immune response, and the ability in reaching the
42 equilibrium phase. This, in turn, motivates the appeal to PDEs descriptions and can complete
43 the already established modeling based on ordinary differential systems, on which there exists a
44 wide literature, see for instance (14, 15, 11, 16, 17, 18, 19) Extension to the PDE framework has
45 permitted to bring out the role of space organisation (20, 21, 22, 23). The reader can find further
46 details and references about the mathematical modeling of tumor-immune system interactions,
47 based on different viewpoints and addressing several issues of the efficacy of the immune
48 response, in the reviews (24, 25, 26, 27, 28, 29). The original model developed in (10) thus
49 accounts for both the growth of the tumor, by natural cell growth and cell divisions, and the
50 displacement of the immune cells towards the tumor, by means of activation processes and
51 chemotaxis effects. The most notable finding from (10) was that an equilibrium state, with
52 residual tumor and active immune cells, can be observed. Moreover, mathematical analysis
53 provides a basis for the explanation of the formation of the equilibrium. How the biological
54 parameters shape this equilibrium is the main question investigated in the present article. Indeed,
55 the equilibrium can be mathematically interpreted by means of an eigenproblem coupled to a
56 stationary diffusion equation with constraint. This observation permits us to develop an efficient
57 numerical strategy to determine *a priori* the shape of the equilibrium — namely, the size
58 distribution of the tumor cells and the residual tumor mass — for a given set of biological
59 tumor and immune cell parameters. Consequently, the equilibrium state can be computed at low
60 numerical cost since we can avoid the resolution of the evolution problem on a long time range.
61 The use of this simple and fast algorithm allows us to address the question of the sensitivity of
62 the residual mass to the parameters and to discuss the impact of treatments. This information
63 can be decisive to design clinical studies and choose therapeutic strategies that will revert to an
64 equilibrium phase. Our work therefore provides hints for cancer treatment management.

65 **Quick guide to equations: A coupled PDE model for tumor-immune system** 66 **interactions**

67 The modeling approach imposes to select a few phenomena, considered as the leading effects
68 for the situation under consideration; other effects are just roughly described by tuning some
69 parameters or are simply disregarded. Choices for designing the mathematical model are also
70 dictated by the difficulty in attributing numerical values to the parameters of the equations,
71 due to a lack of experimental measurements: the poor knowledge of driving quantities leads to
72 keep a description as simple as possible, with a reduced number of unknown parameters. The
73 principles of the modeling adopted in (10), summarized by **Fig. 1**, led to couple an evolution
74 equation for the size-distribution of the tumor cells, and a convection-diffusion equation for the
75 activated immune cells. The two-way coupling arises from the death term induced by the action
76 of the immune cells on the tumor cells, and by the activation and the attraction of immune cells
77 towards the tumor, which are determined by the total mass of the tumor. The model is intended

78 to describe the earliest stages of the tumor formation, when the size of the tumor is relatively
 79 small. The tumor is located at the center of a domain Ω (there is no displacement of the tumor).
 80 The model distinguishes two distinct and independent length scales: the size of the tumor cells,
 81 described by the variable $z \geq 0$, is considered as “infinitely small” compared to the scale of
 82 displacement of the immune cells, described by the space variable $x \in \Omega$.

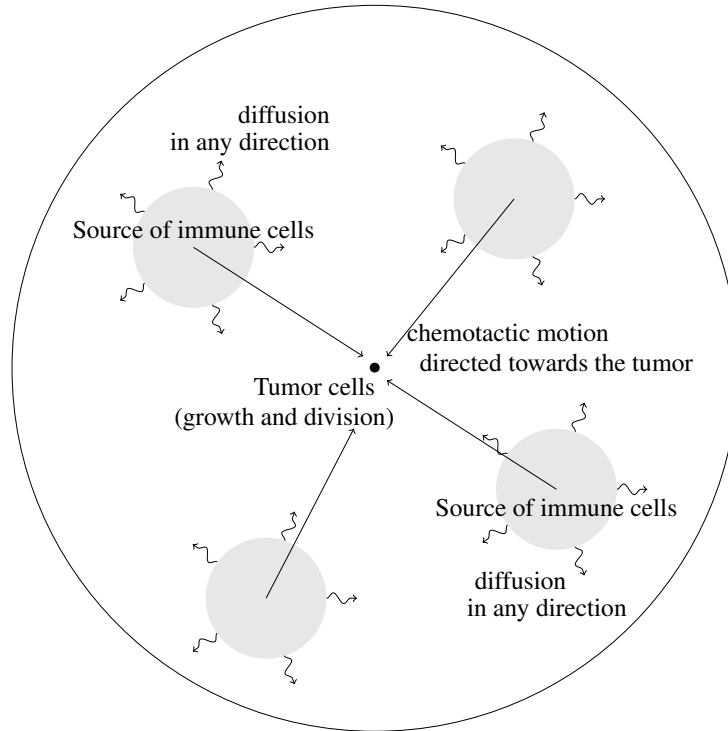


Figure 1. Schematic view of the geometry of the mathematical model. The tumor cells are located at the center of the domain where they are subjected to growth and division mechanisms. Immune cells are activated from baths of resting cells; their motion is driven by diffusion combined to a convection field, due to chemotactic mechanisms and directed towards the tumor.

83 The unknowns are

- 84 •the size density of tumor cells $(t, z) \mapsto n(t, z)$ so that the integral $\int_a^b zn(t, z) dz$ gives the
- 85 volume of the tumor occupied at time t by cells having their size z in the interval (a, b) ;
- 86 •the concentration of activated immune cells which are fighting against the tumor $(t, x) \mapsto$
- 87 $c(t, x)$;
- 88 •the concentration of chemical signal that attracts the immune cells towards the tumor
- 89 microenvironment $(t, x) \mapsto \phi(t, x)$.

90 The specific biological assumptions made to construct the model are fully described in (10).
 91 **Fig. 2** offers an overview of the interaction mechanisms embodied in the equations and of the
 92 role of the parameters of the model.

93 Immune cells, once activated from a bath of resting cells, are subjected to natural diffusion and
 94 to a chemotactic drift, induced by the presence of the tumor. The strength of this drift, as well as

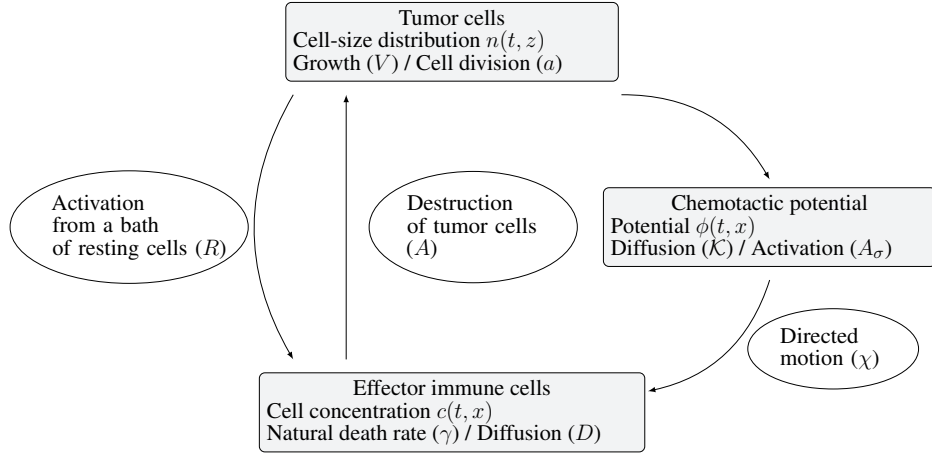


Figure 2. Schematic view of the interaction mechanisms described by the system (1a)-(1e)

95 the activation of immune cells, directly depends on the total mass of the tumor, proportional to
 96 the quantity

$$\mu_1(t) = \int_0^\infty zn(t, z) dz.$$

The immune system-tumor competition is described by the following system of PDEs

$$\partial_t n + \partial_z(Vn) = Q(n) - m(n, c), \quad (1a)$$

$$\partial_t c + \nabla_x \cdot (c\chi \nabla_x \phi - D \nabla_x c) = \mu_1 R - \gamma c, \quad (1b)$$

$$- \mathcal{K} \Delta_x \phi = \mu_1 \left(\sigma(x) - \frac{1}{|\Omega|} \int_\Omega \sigma(y) dy \right), \quad (1c)$$

$$n(t, 0) = 0, \quad c|_{\partial\Omega} = 0, \quad \mathcal{K} \nabla_x \phi \cdot \nu|_{\partial\Omega} = 0, \quad (1d)$$

$$n(t=0, z) = n_0(z), \quad c(t=0, x) = c_0(x). \quad (1e)$$

97 The features of the growth-division dynamics for the tumor cells (1a) are embodied into the
 98 (possibly size-dependent) growth rate $z \mapsto V(z) \geq 0$ and the cell division operator $Q(n)$. We
 99 refer the reader to (30, 31, 32, 33, 34, 35, 36, 37) for further details on this evolution equation
 100 (with $m(n, c) = 0$) for cell growth and division, and its application to cancer modeling. What is
 101 crucial for modeling purposes is the principle that cell-division does not change the total mass:
 102 the operator Q satisfies $\int_0^\infty zQ(n) dz = 0$. However, the total number of cells in the tumor
 103 increases since $\int_0^\infty Q(n) dz \geq 0$ (we refer the reader to (10) and Appendix 1 for further details).
 104 In what follows, we restrict to the mere symmetric binary division operator

$$Q(n)(t, z) = a(z)(4n(t, 2z) - n(t, z)), \quad (2)$$

105 with $z \mapsto a(z) \geq 0$ the division rate. It simply describes the situation where cells are cut into
 106 two cells having half the size of the original cell. Further relevant examples of division operators
 107 can be found in (32) (see Appendix 1). The specific case where the division rate a in (2) is a

108 positive constant makes the model simpler, and is often used. It is however likely relevant to
 109 incorporate more complex behaviors through the size-dependence; for instance divisions can
 110 be prohibited below a certain size threshold. Similarly, it can be convenient to assume that
 111 the growth rate V is a positive constant, but more intricate laws can take into account some
 112 important phenomena. For instance, logistic or Gompertz law can incorporate size limitation
 113 effects, and roughly describe difficulties in accessing nutrients or necrotic effects (38, 39, 40); a
 114 detailed study of growth laws can be found in (41). As mentioned above, though, using such
 115 complex laws, also raises the issue of determining more parameters. The boundary condition for
 116 n in (1d) means that no tumor cells are created with size 0.

117 Despite the fact that there exists several types of immune cells – at least T-cells and NK cells –
 118 fighting against the tumor, they are all described here through the single concentration c . It also
 119 means that coefficients of the equation – the death rate $\gamma > 0$, the chemotactic strength $\chi > 0$,
 120 and the diffusion coefficient D – correspond to an averaged behavior of all these cells. By the
 121 way, working with a constant diffusion coefficient $D > 0$ is again a simplification, neglecting
 122 the architecture of the tumor environment, which might induce directional effects. The effector
 123 immune cells that effectively fight against the tumor, are activated from a “reservoir” of resting
 124 cells, described in the right hand side of (1b) by $(t, x) \mapsto R(t, x)$. This given function, possibly
 125 time and space dependent, stands for the space distribution of the influx rate of activated effector
 126 immune cells. It takes into account the sources of resting immune cells that can be activated in
 127 the tumor microenvironment or in the draining lymph nodes into cells fighting the tumor. At early
 128 stages of tumor growth, the rate of the activation process is supposed to be directly proportional to
 129 the tumor mass μ_1 . Again, more complex activation law, for instance based on Michaelis-Menten
 130 kinetics can incorporate relevant limitation mechanisms. The Dirichlet boundary condition for
 131 c in (1d) means that the immune cells far from the tumor are non-activated. Immune cells are
 132 directed towards the tumor by a chemo-attractive potential ϕ , induced by the presence of the
 133 tumor cells. Through (1c), the strength of the signal is proportional to the total mass of the tumor,
 134 and it is shaped by a form function $x \mapsto \sigma(x)$ which will be a function peaked at the tumor
 135 location. The potential is thus defined by the diffusion equation (1c), that involves a positive
 136 coefficient $\mathcal{K} > 0$ (that could be matrix valued), and the Neumann boundary condition in (1d),
 137 where ν stands for the unit outward normal vector on $\partial\Omega$. Finally, the activated immune cells
 138 are able to destroy tumor cells, as described by the death term in (1a)

$$m(c, n)(t, z) = \underbrace{\int_{\Omega} \delta(y)c(t, y) dy}_{:=\mu_c(t)} \times n(t, z), \quad (3)$$

139 where $\delta \geq 0$ is another form function, also peaked in the vicinity of the tumor. For the numerical
 140 experiments, we shall work with the Gaussian profiles

$$\delta(x) = \frac{A}{\theta\sqrt{2\pi}} \exp\left(-\frac{|x|^2}{2\theta^2}\right), \quad \sigma(x) = \frac{A_\sigma}{\theta_\sigma\sqrt{2\pi}} \exp\left(-\frac{|x|^2}{2\theta_\sigma^2}\right), \quad (4)$$

141 where the positive parameters A, A_σ and θ, θ_σ can be used to tune the amplitude and spreading
 142 of these functions, and thus the strength and radius of influence of the related phenomena.
 143 We refer the reader to (10) for further details and comments about the model. Note that this

144 model neglects the possible additional protumoral effects that can take place and are crucial to
 145 swing to the escape phase. Such protumor effects can have different forms: they can directly
 146 enhance the tumor growth, and make antitumor immune cells exhausted, a state where they
 147 are hyporesponsive and cannot kill the tumor, see (42) on these issues. Remarkably, the model
 148 (1a)-(1e) is able to reproduce equilibrium phases where the tumor growth is controlled by the
 149 immune response.

2 MATERIALS AND METHODS

150 2.1 Development of numerical methods predicting parameters of the 151 equilibrium in immune-controlled tumors

152 According to (2, 3, 9), the equilibrium phase corresponds to a long-lasting period of immune-
 153 mediated latency, also known as tumor mass dormancy, prior to the emergence of clinically
 154 detectable malignant disease, with a residual tumor which has not be fully destroyed by the
 155 immune system, maintained under the control of immunity. The simulations of the initial-
 156 boundary value problem (1a)-(1e) performed in (10) revealed that such a behavior can be
 157 reproduced by the model. Here, we wish to study the features of the equilibrium phase in
 158 immune-controlled tumors and, in particular, we want to predict, for given biological parameters
 159 (see Section 2.2 below), the total mass of the residual tumor and its size distribution. To this
 160 end, we developed specific numerical procedures based on the mathematical interpretation of
 161 the equilibrium.

162 2.1.1 Equilibrium states

163 The definition of the equilibrium relies on the following arguments. When disregarding the
 164 immune response, the cell-division equation

$$\partial_t n + \partial_z(Vn) = Q(n). \quad (5)$$

165 admits a positive eigenstate, which drives the large time behavior of the solution. To be more
 166 specific, there exists $\lambda > 0$ and a non negative function $z \geq 0 \mapsto \bar{N}(z)$ satisfying

$$\begin{cases} \partial_z(V\bar{N}) - Q(\bar{N}) + \lambda\bar{N} = 0 \text{ for } z \geq 0 \\ \bar{N}(0) = 0, \quad \bar{N}(z) > 0 \text{ for } z > 0, \quad \int_0^{+\infty} \bar{N}(z) dz = 1. \end{cases} \quad (6)$$

The existence-uniqueness of the eigenpair (λ, \bar{N}) can be found in (32, 34). Furthermore, when
 the tumor does not interact with the immune system, the large time behavior is precisely driven
 by the eigenpair: the solution of (5) behaves like

$$n(t, z) \underset{t \rightarrow \infty}{\sim} \mu_0 e^{\lambda t} \bar{N}(z)$$

167 where $\mu_0 > 0$ is a constant determined by the initial condition, see (34, 33). Consequently, in
 168 the immune-free case, the tumor population grows exponentially fast, with a rate $\lambda > 0$, and, as
 169 time becomes large, its size repartition obeys a certain profile \bar{N} . In the specific case where V is
 170 constant and Q is the binary division operator (2), with a constant division rate a , we simply

171 have $\lambda = a$ and the profile \bar{N} is explicitly known, (43, 44). However, for general growth rates
 172 and division kernels the solution should be determined by numerical approximations; we are
 173 going to detail a numerical procedure to effectively compute the pair (λ, \bar{N}) .
 174

175 Coming back to the coupled model (1a)-(1e), we infer that the equilibrium phase corresponds
 176 to the situation where the death rate – the integral of the immune cells concentration with weight
 177 δ , denoted as $\bar{\mu}_c$ in (3) – precisely counterbalances the natural exponential growth of the tumor
 178 cell population. In other words, at equilibrium we expect that

- 179 •the size distribution of tumor cells is proportional to the eigenstate $\mu_0 \bar{N}(z)$. The
- 180 proportionality factor is related to the total mass by the relation $\mu_1 = \mu_0 \int_0^\infty z \bar{N}(z) dz$.
- 181 •the concentration of immune cells is defined by the stationary equation

$$\gamma C - \nabla_x \cdot (D \nabla_x C) + \mu_1 \nabla_x \cdot (\chi C \nabla_x \Phi) = \mu_1 R, \quad C|_{\partial\Omega=0} = 0, \quad (7)$$

where Φ is the solution of

$$-\mathcal{K} \Delta_x \Phi = \sigma - \frac{1}{|\Omega|} \int_{\Omega} \sigma(y) dy,$$

182 endowed with the homogeneous Neumann boundary condition, together with the constraint

$$\int_{\Omega} \delta(x) C(x) dx = \lambda. \quad (8)$$

183 This can be interpreted as an implicit definition of the total mass μ_1 to be the value such that the
 184 solution of the boundary value problem (7) satisfies (8): in other words, it defines implicitly the
 185 mass of the residual tumor μ_1 to be the value such that the solution of the stationary boundary
 186 value problem for C defines a death rate that exactly compensates the exponential growth rate
 187 of the growth division equation. The existence of an equilibrium state defined in this way is
 188 rigorously justified in (10, Theorem 2).

189 **THEOREM 2.1.** *Let $x \mapsto R(x) \in L^2(\Omega)$ be a non negative function. If $\lambda > 0$ is small enough,*
 190 *there exists a unique $\mu_1(\lambda) > 0$ such that the solution $C_{\mu_1(\lambda)}$ of the stationary equation (7)*
 191 *satisfies (8).*

192 Theorem 2.1 requires a smallness assumption; for (2) with constant growth rate V and division
 193 rate a , this is a smallness assumption on a . Numerical experiments have shown different large
 194 time behaviors for the initial-boundary value problem (1a)-(1e) (an example will be presented
 195 later on):

- 196 •when the source term R is space-homogeneous, the expected behavior seems to be very robust.
- 197 The immune cell concentration tends to fulfill the constraint $\bar{\mu}_c(t) \sim \lambda$ as time becomes large,
- 198 and the size repartition of tumor cells tends to the eigenfunction \bar{N} . The total mass μ_1 tends to
- 199 a constant; however the asymptotic value cannot be predicted easily.
- 200 •When R has space variations, the asymptotic behavior seems to be much more sensitive to the
- 201 parameters of the model, in particular to the aggressiveness of the tumor (characterized by the

202 cell division rate a). On short time scale of simulations, we observe alternance of growth and
203 remission phases, and the damping to the equilibrium could be very slow.

204 These observations bring out the complementary roles of different type of cytotoxic cells (45).
205 The NK cells could be seen as a space-homogenous source of immune cells, immediately
206 available to fight against the tumor, at the early stage of tumor growth. In contrast, T-cells need
207 an efficient priming which occurs in the draining lymph nodes, and their sources is therefore
208 non-homogeneously distributed. Eventually, NK and $CD8^+$ T-cells cooperate to the anti-tumor
209 immune response.

210

211 Numerical experiments thus show that the model (1a)–(1e) is able to reproduce, in the long-
212 time range, cancer-persistent equilibrium, but the features of the equilibrium, and its ability to
213 establish, are highly sensitive to the parameters. To discuss this issue further, we focus here
214 on the mass at equilibrium considered as a critical quantity that evaluates the efficacy of the
215 immune response. Indeed, it is known that a tumor gains in malignancy when its mass reaches
216 certain thresholds (45, 46). The smaller the tumor mass at equilibrium, the better the vital
217 prognosis of the patient. In doing so, we do not consider transient states and time necessary for
218 the equilibrium to establish. The interest of the interpretation of the equilibrium by means of
219 an eigenproblem relies on the fact that the equilibrium state can be determined a priori, at least
220 through numerical simulations, without running the initial boundary value problem over long
221 time ranges: given a set of biological parameters it can be obtained by solving the eigenvalue
222 problem for (λ, \bar{N}) and the constrained stationary drift-diffusion equation for C , see **Fig. 3**.
223 In turn, since the equilibrium state can be computed at low numerical cost, a wide range of
224 parameters can be considered and the role of the parameters can be investigated in details. The
225 determination, on numerical grounds, of the equilibrium state relies on a two-step process, as
226 schematised in **Fig. 3**. First, we compute the normalized eigenstate of the tumor cell equation,
227 second, we find the tumor mass which makes the coupled death rate fit with the eigenvalue. To
228 this end, we have developed a specific numerical approach.

229 2.1.2 The eigen-elements of the growth-division equation

230 The numerical procedure is fully detailed and analyzed in Appendix 1; it is inspired from the
231 spectral analysis of the equation: λ is found as the leading eigenvalue of a conveniently shifted
232 version of the growth-division operator. In practice, we work with a problem where the size
233 variable is both truncated and discretized. Hence, the problem recasts as finding the leading
234 eigenvalue of a shifted version of the underlying matrix, which can be addressed by using the
235 inverse power method (47, Section 1.2.5). We refer the reader to (48, 49) for a thorough analysis
236 of the approximation of eigenproblems for differential and integral operators, which provides
237 a rigorous basis to this approach. It is also important to check a priori, based on the analysis
238 of the equation (32), how large the shift should be, and that it remains independent on the
239 numerical parameters. As already mentioned, for some specific division and growth rates, the
240 eigenpair (λ, \bar{N}) is explicitly known, see (32). We used these formula to validate the ability of
241 the algorithm to find the expected values and profiles.

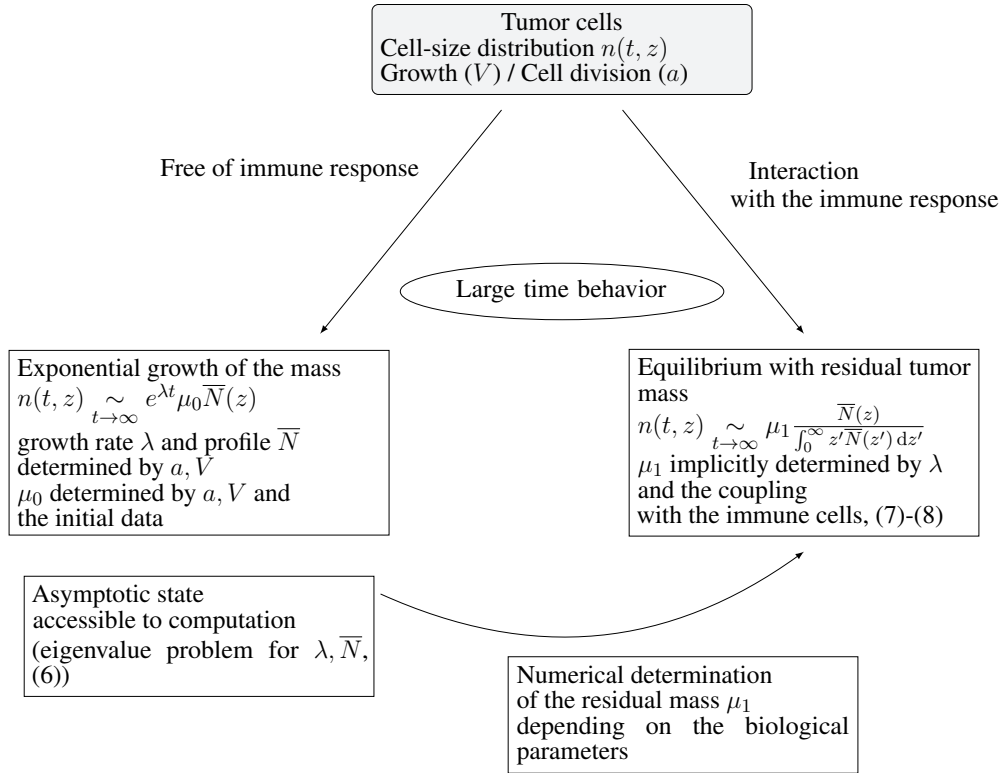


Figure 3. Connection of the equilibrium state with the eigenstate of the growth-division equation, and interpretation of the residual tumor mass.

242 2.1.3 Computation of the equilibrium mass

243 Having at hand the eigenvalue λ , we go back to the convection-diffusion equation (7) and the
 244 constraint (8) that determine implicitly the total mass μ_1 of the residual tumor. For a given value
 245 of μ_1 , we numerically solve (7) by using a finite volume scheme, see (10, Appendix C). Then,
 246 we use the dichotomy algorithm to fit the constraint:

- 247 •The chemo-attractive potential Φ is computed once for all.
- 248 •Pick two reference values $0 < \mu_a < \mu_b$; the mass we are searching for is expected to belong to
 249 the interval (μ_a, μ_b) .
- 250 •Set $\mu_1 = \frac{\mu_a + \mu_b}{2}$ and compute the associated solution C_{μ_1} of (7) (the subscript emphasizes the
 251 dependence with respect to μ_1). Evaluate the discrete version of the quantity $I = \int \delta C_{\mu_1} dx -$
 252 λ .
- 253 •If $I < 0$, then replace μ_a by μ_1 , otherwise replace μ_b by μ_1 .
- 254 •We stop the algorithm when the relative error $\frac{\mu_b - \mu_a}{\mu_a} < \epsilon$ is small enough.

255 It is also possible to design an algorithm based on the Newton method. However, this approach
 256 is much more numerically demanding (it requires to solve more convection-diffusion equations)
 257 and does not provide better results.

258 2.2 Identification of biological parameters

259 In order to go beyond the qualitative discussion of (10), the model should be challenged with
 260 biological data. The PDE system (1a)-(1e) is governed by the set of parameters collected in
 261 **Table 1**. Most parameter values were retrieved from previously published experimental results
 262 and we propose an estimation of the remaining parameters R, a, V based on the experimental
 263 study performed in (50) where the development of chemically-induced cutaneous squamous cell
 264 carcinoma (cSCC) is investigated.

Symbol	Description	Value and unit	References
χ	chemotactic coefficient	$8.64 \times 10^1 - 8.64 \times 10^6 \text{ mm}^2 \cdot \text{mmol}^{-1} \cdot \text{day}^{-1}$	(Macrophages) (51)
D	natural space diffusion coef. of the cytotoxic effector cells population	$8.64 \times 10^{-5} - 10^{-3} \text{ mm}^2 \cdot \text{day}^{-1}$	(CD8 ⁺ T-cells) (52), (23)
R	the normal rate of influx of effector immune cells	$\log(R) \sim \mathcal{N}(\log(2.2 \times 10^{-6}), 0.84) \left(\frac{\text{cell}_n \cdot \text{mm}^{-3}}{\text{cell}_n \cdot \mu\text{m}^3} \cdot \text{day}^{-1} \right)$	estimated
γ	natural death rate of the tumor antigen-specific cytotoxic effector cells	$2 \times 10^{-2} - 1 \text{ day}^{-1}$	(53), (20), (14), (22)
A	strength of the immune response	$2 - 57.6 \text{ cell}_n^{-1} \cdot \text{day}^{-1}$	(54), (55), (56), (57)
K	diffusion coefficient for the attractive potential ϕ	$10^{-2} - 1 \text{ mm}^2 \cdot \text{day}^{-1}$	(58), (23)
A_σ	strength of the chemical signal induced by each tumor cell	$5 \cdot 10^{-17} - 0.625 \times 10^{-16} \text{ mmol} \cdot \mu\text{m}^3 \cdot \text{day}^{-1}$	(59)
a	division rate of the tumor cells	$\log(a) \sim \mathcal{N}(\log(0.12), 0.2) \text{ (} a \text{ in } \text{day}^{-1}\text{)}$	estimated
V	growth rate of the tumor cells	$\log(V) \sim \mathcal{N}(\log(816.33), 0.51) \text{ (} V \text{ in } \mu\text{m}^3 \cdot \text{day}^{-1}\text{)}$	estimated

Table 1. Key model parameters and their biophysical meaning

265 Calibrating the parameters of the equations is an issue due to the lack of direct measurements,
 266 and the fact that experimental data are obtained at the price of the sacrifice of mice. Consequently,
 267 beyond the cost of the experiments, it also means that a time evolution of the quantities of interest
 268 is usually not affordable. Therefore, a specific procedure should be developed in order to estimate
 269 the parameters from the experimental data points. Since the informations on the parameters are
 270 quite poor, we restrict to the case where the coefficients a, V, R are constant, which is also a
 271 reasonable assumption when dealing with the earliest stages of the tumor development. In order
 272 to identify the parameters, we shall use a degraded version of the equations.

273 Neglecting the immune response, the tumor growth is driven by (5). As explained above,
 274 this leads to an exponential growth of the tumor mass, see (32, 34, 33, 44). Let $t \mapsto \mu_0(t) =$
 275 $\int_0^\infty n(t, z) dz$, the total number of tumor cells, and $t \mapsto \mu_1(t) = \int_0^\infty zn(t, z) dz$. Integrating (5)
 276 with respect to size variable, with integration by parts, and bearing in mind that the cell division
 277 operator is mass preserving, we thus get

$$\frac{d}{dt}\mu_0 = a\mu_0, \quad \frac{d}{dt}\mu_1 = V\mu_0. \quad (9)$$

278 Next, assuming space homogeneity of the immune cells concentration and neglecting the
 279 displacement and the natural death rate of the immune cells, the immune cells concentration is
 280 driven by

$$\frac{d}{dt}c = R\mu_1. \quad (10)$$

281 Based on this simplified dynamics, reduced to (9)-(10), we used the Nonlinear Mixed Effects
 282 Modeling (NMEM) in order to estimate the parameters a, V, R from the experimental data. Let
 283 N denote the number of mice within the population and $Y_i^{(k)} = \{y_{i1}^{(k)}, \dots, y_{in_i}^{(k)}\}$ the vector of
 284 longitudinal measurements for the i th mouse: $y_{ij}^{(k)}$ is a typical observation of the mouse i for a
 285 given measurement type $k \in \{0, 1, 2\}$ (with $(0, 1, 2)$ referring to (μ_0, μ_1, c) respectively) at time
 286 t_{ij}^k for $i \in \{1, \dots, N\}$ and $j \in \{1, \dots, n_i^k\}$. We suppose that the statistics of the measurements
 287 obeys, for $k \in \{0, 1, 2\}$, $j \in \{1, \dots, n_i^k\}$, $i \in \{1, \dots, N\}$,

$$y_{ij}^{(k)} = f^{(k)}(t_{ij}^k; \theta_i^k) + e_{ij}^{(k)}, \quad (11)$$

288 where $f^{(k)}(t_{ij}^k; \theta_i^k)$ is the evaluation of the model at time t_{ij}^k , $\theta_i^k \in \mathbb{R}^p$ is the vector of the
 289 parameters describing the individual i and $e_{ij}^{(k)}$ the residual error model. The inter-individual
 290 variability is described by the combination of fixed effects θ_{pop}^k , which, by definition, are
 291 constant within the population and along time, and random effects η_i^k which explain the inter-
 292 individual variability among the mice. The positivity of the parameters is ensured by assuming
 293 that the individual parameters follow a log-normal distribution. In other words, the random
 294 effects are normally distributed with mean zero and a variance-covariance matrix \mathcal{W} . For
 295 instance $\mathcal{W} = \text{diag}(\omega^0, \omega^1, \omega^2)$ where the ω^k 's stand for the variance of the parameters a, V, R .
 296 Therefore, we have

$$\log \theta_i^k = \log(\theta_{pop}^k) + \eta_i^k, \quad \eta_i^k \sim \mathcal{N}(0, \omega^k) \quad (12)$$

297 for $k \in \{0, 1, 2\}$. The error model is assumed to be proportional to the model evaluation and is
 298 defined as follows:

$$e_{ij}^{(k)} = \left(b^{(k)} f^{(k)}(t_{ij}^k; \theta_i^k) \right) \varepsilon_{ij} \quad (13)$$

299 where $\varepsilon_{ij} \sim \mathcal{N}(0, 1)$ represents the statistical model residual errors and $b^{(k)}$ is the proportionality
 300 factor measuring the relative amplitude of the errors.

301

Estimation of the model parameters. According to the experimental procedure in (50), 5×10^5 mSCC38 were injected to each mouse at time $t_0 = 0$. Therefore we fixed the initial number of tumor cells to $\mu_0(0) = 5 \times 10^5$ cells. Assuming that each tumor cell is spherically shaped with a radius $15 \mu m$, we set $\mu_1(0) = 7.1 \text{ mm}^3$. The initial concentration of immune cells is fixed to $c_0 = 0$: we suppose that initially there is no effector immune cells (or at least it means that the initial concentration of activated immune cells is negligible compared to the concentration of resting cells). Some data points were censored due to the sacrifice of the individual for flow cytometry cell counting. The censored data points have been handled by Limit Of Quantification (LOQ) censoring (60). Let I_{ij}^k be the finite or infinite censoring interval

for mouse i , measurement k and time t_{ij}^k and

$$\mathbb{P}(y_{ij}^{(k)} \in I_{ij}^k | \theta_i^k) = \int_{I_{ij}^k} p_{y_{ij}^{(k)} | \theta_i^k}(x | \theta_i^k) dx,$$

302 where $p_{y_{ij}^{(k)} | \theta_i^k}$ is the conditional distribution of $y_{ij}^{(k)}$ given θ_i^k . Let us collect in a vector $\alpha =$
 303 $(a_{pop}, V_{pop}, R_{pop}, \omega_a, \omega_V, \omega_R, b_a, b_V, b_R)$ the parameters of the model; they are estimated by
 304 maximizing the observed likelihood function

$$\begin{aligned} \mathcal{L}(\alpha, y) = & \prod_{k=0}^2 \prod_{i=1}^N \prod_{j=1}^{n_i^k} \int p(y_{ij}^{(k)} | \theta_i^k) \mathbf{1}_{\{y_{ij}^{(k)} \notin I_{ij}^k\}} \\ & \times \mathbb{P}(y_{ij}^{(k)} \in I_{ij}^k | \theta_i^k) \mathbf{1}_{\{y_{ij}^{(k)} \in I_{ij}^k\}} p(\theta_i^k; \alpha) d\theta_i^k. \end{aligned} \quad (14)$$

305 To this end, we used the Stochastic Approximation of the Expectation Maximization algorithm
 306 (SAEM) implemented in the MONOLIX R API (61). Furthermore, the individual parameter
 307 estimators $\hat{\theta}_i^k$ are computed in MONOLIX (61) by means of the Empirical Bayes Estimate
 308 (EBE) of θ_i^k which corresponds to the mode of the conditional distribution $p(\theta_i^k | y_i^k; \hat{\alpha})$ (where $\hat{\alpha}$
 309 corresponds to estimated parameters).

310

311 A preliminary estimation procedure indicates a significant correlation between the parameters a
 312 and R (t-test p-value 2.6×10^{-6}). Hence, introducing this correlation into the variance covariance
 313 matrix of the random effects by setting $\text{covar}(a, R) = \rho_{aR} \omega_a \omega_R$, where ρ_{aR} represents the
 314 correlation coefficient between a and R , enhances the goodness of fit. The estimated value
 315 of ρ_{aR} is 0.8 with a relative standard error of 13%. The parameters in α were estimated with
 316 reasonable standard errors (computed using the stochastic approximation) and relative standard
 317 errors ($\max(R.S.E.) = 30.6$ and $\min(R.S.E.) = 3$) which indicate that the model parameters
 318 are identifiable. The Shapiro Wilk test reinforces the normality hypotheses on the random effects
 319 $\eta_i^{(k)}$ (the p-values for η_a, η_V and η_R are respectively 0.83, 0.61, 0.2). Pictures indicating the fits
 320 are provided in **Fig. 4**, and detailed parameter estimates are given in **Table 2**.

parameters	value	S.E	R.S.E (%)
a_{pop}	0.12	0.0041	3
V_{pop}	816.33	92.59	11
R_{pop}	2.2×10^{-6}	3.6×10^{-7}	16
ω_a	0.20	0.027	13.5
ω_V	0.51	0.075	15
ω_R	0.84	0.11	13
b_a	0.37	0.041	11
b_V	0.17	0.052	31
b_R	0.18	0.056	30
ρ_{aR}	0.8	0.1	13

Table 2. Estimated value of the parameters with their Standard Error (S.E.) and Relative Standard Error (R.S.E)

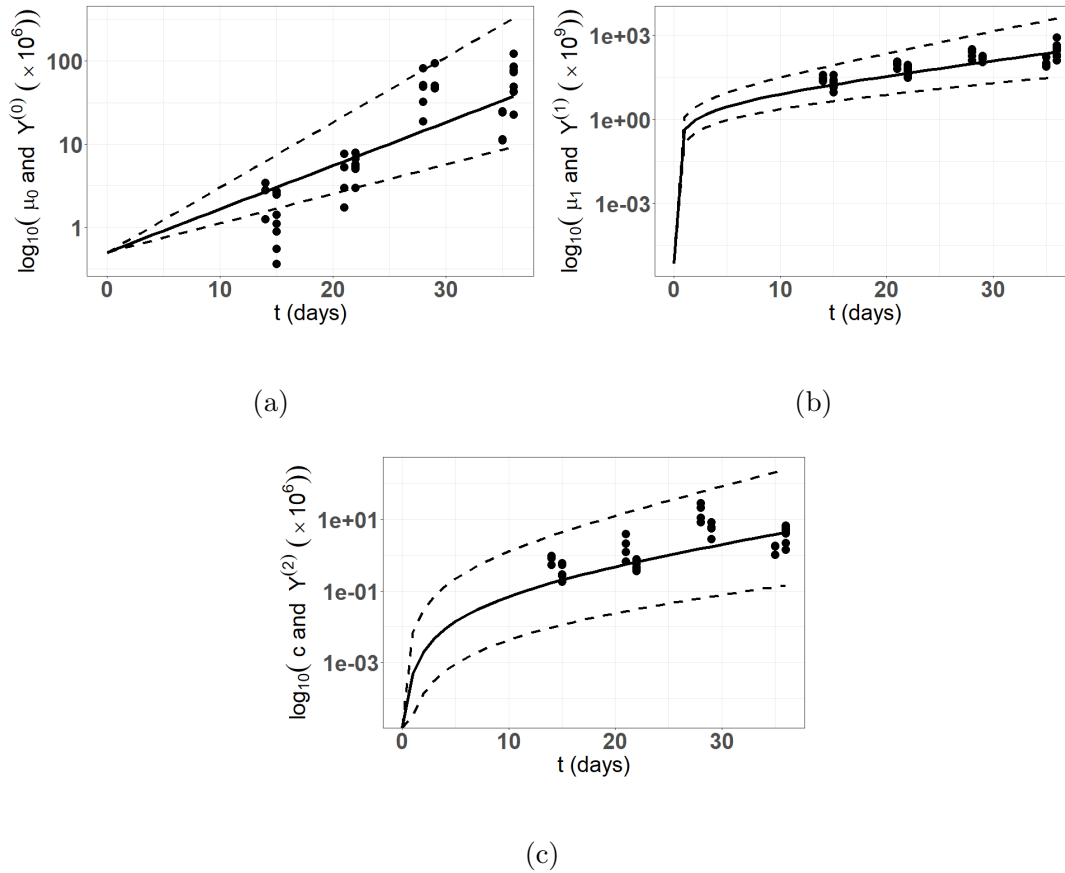


Figure 4. Model fitting to the in vivo experimental cSCC tumor growth data. Here, we are using 34 data points from an in vivo experimental cutaneous squamous cell carcinoma (cSCC) tumor growth mouse model (50). **(a):** Number of tumor cells kinetics; **(b):** Tumor volume kinetics (μm^3); **(c):** Concentration of immune cells kinetics. The solid lines represent the model prediction using the mean estimated parameters, the dashed lines represent the model predictions using the 5th and 95th percentiles of the parameters distribution

321 2.3 Materials

322 **Mice.** FVB/N wild-type (WT) mice (Charles River Laboratories, St Germain Nuelles, France)
 323 were bred and housed in specific-pathogen-free conditions. Experiments were performed using
 324 6-7 week-old female FVB/N, in compliance with institutional guidelines and have been approved
 325 by the regional committee for animal experimentation (reference MESR 2016112515599520;
 326 CIEPAL, Nice Côte d'Azur, France).
 327

328 **In vivo tumor growth.** mSCC38 tumor cell line was established from DMBA/PMA induced
 329 sSCCs and maintained in DMEM (Gibco-ThermoFisher Scientific, Courtaboeuf, France)
 330 supplemented with 10% heat-inactivated fetal bovine serum (FBS) (GE Healthcare, Chicago,
 331 Illinois, USA) penicillin (100 U/ml) and streptomycin (100 $\mu g/ml$) (Gibco-ThermoFisher

332 Scientific, Courtaboeuf, France). 5×10^5 mSCC38 were intradermally injected in anesthetized
 333 mice after dorsal skin shaving. Tumor volume was measured manually using a ruler and
 334 calculated according to the ellipsoid formula: $\text{Volume} = \text{Length (mm)} \times \text{Width (mm)} \times \text{Height}$
 335 $(\text{mm}) \times \pi/6$.
 336

337 **Tissue preparation and cell count.** mSCC38 were excised and enzymatically treated twice
 338 with collagenase IV (1 mg/ml) (Sigma-Aldrich, St Quentin Fallavier, France), and DNase I
 339 (0.2 mg/ml) (Roche Diagnostic, Meylan, France) for 20 minutes at 37° C . Total cell count was
 340 obtained on a Casy cell counter (Ovni Life Science, Bremen, Germany). Immune cell count was
 341 determined from flow cytometry analysis. Briefly, cell suspensions were incubated with anti-
 342 CD16/32 (2.4G2) to block Fc receptors and stained with anti-CD45 (30-F11)-BV510 antibody
 343 and the 7-Aminoactinomycin D (7-AAD) to identify live immune cells (BD Biosciences, Le
 344 Pont de Claix, France). Samples were acquired on a BD LSR Fortessa and analyzed with DIVA
 345 V8 and FlowJo V10 software (BD Biosciences, Le Pont de Claix, France).
 346

347 **Mathematical and statistical analysis.** Computations were realized in `Python` and we made
 348 use of dedicated libraries, in particular the `gmsh` library for the computational domain mesh
 349 generation, the packages `optimize` (for the the optimization methods using the Levenberg-
 350 Marquard mean square algorithm; similar results have been obtained with the CMA-ES
 351 algorithm of the library `cma`) from the library `scipy`, the `MONOLIX R API` and application
 352 for the model calibration to the experimental data (61), the library `Pygpc` for the generalized
 353 Polynomial Chaos approximation (62) and the library `Salib` for the sensitivity analysis (63).

3 RESULTS

354 3.1 Validation of the method

355 For all the simulations discussed here, we adopt the same framework as in (10): the tumor
 356 is located at the origin of the computational domain Ω , which is the two-dimensional unit
 357 disk. Otherwise explicitly stated, we work with the lower bound of the parameters collected in
 358 **Table 1**. When necessary, the initial values of the unknowns are respectively $\mu_0(0) = 1 \text{ cell}_n$,
 359 $\mu_1(0) = 14137.2 \mu\text{m}^3$, $c(0, x) = 0$.
 360

To start with, we perform a simulation of the initial-boundary value problem (1a)-(1e).
Fig. 5 illustrates how the equilibrium establishes in time: as time becomes large, the effective
 concentration of active immune cells, that is denoted

$$\bar{\mu}_c(t) = \int_{\Omega} \delta(x) c(t, x) dx$$

361 tends to the eigenvalue of the cell-division equation, the total mass $\mu_1(t)$ tends to a constant
 362 and the size distribution of tumor cells takes the profile of the corresponding eigenstate. This
 363 result has been obtained by setting $(a, V, R) = (0.072, 713.61, 1.74 \times 10^{-7})$. We observe a non
 364 symmetric shape of the size distribution of tumor cells, peaked about a diameter of $23 \mu\text{m}$,

365 which is consistent with observational data reporting the mean size distribution of cancer cells
 366 (64, 65).

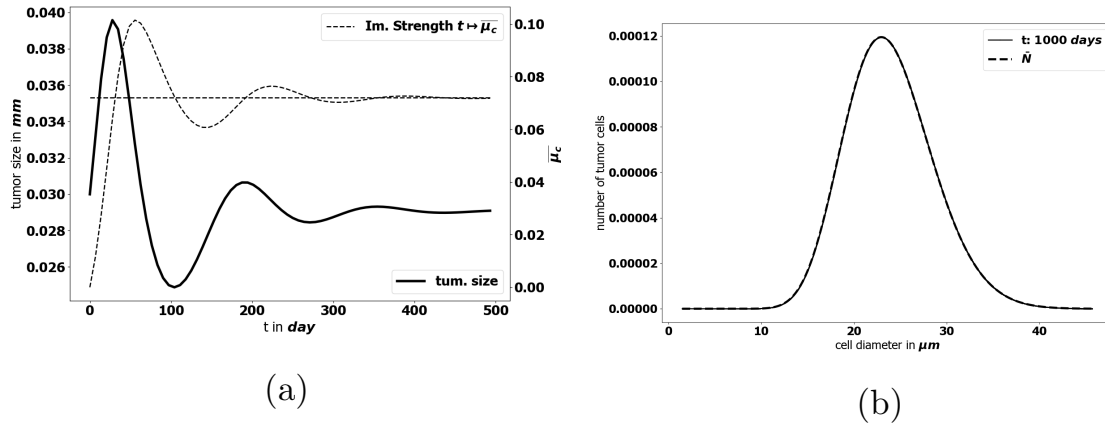


Figure 5. (a): Time evolution of the diameter of the tumor (bold black line) and concentration of active immune cells (dotted gray line). The predicted asymptotic value for the latter is represented by the horizontal dotted line. (b): Comparison of the tumor cell-size distribution at $t = 1000$ days with the positive eigenstate of the cell division equation (x-axis: size of the tumor cells, y-axis: number of tumor cells at the final time). For this simulation $\Omega = \{\|x\| \leq 1\}$, the data are given by the lower bound of the parameters collected in **Table 1** and $(a, V, \bar{R}) = (0.072, 713.61, 1.74 \times 10^{-7})$

For the simplest model of growth-division with a and V constant, we know an expression of the eigenstate (λ, \bar{N}) ; however, we do not know an explicit evaluation of the residual mass. Nevertheless, we can compare the results of the inverse power-dichotomy procedure that predicts the residual mass, to the large time simulations as performed in (10). Let μ_1^f be the asymptotic value of the total mass given by the large time simulation of the initial-boundary value problem (and checking that the variation of the total mass has become negligible) and let μ_1^{pd} be the mass predicted by the power-dichotomy procedure. We set

$$E_{\mu_1} = \frac{|\mu_1^f - \mu_1^{pd}|}{\mu_1^f}.$$

367 The results for several cell division rates a are collected in **Table 3**: the numerical procedures
 368 finds the same equilibrium mass as the resolution of the evolution problem, which is a further
 369 validation of the method.

370 Further validation concerning the ability in finding the leading eigenstate are presented in
 371 Appendix 1. The method has been successfully employed to predict equilibrium state when
 372 dealing with complex growth rate and division operator in (42).

a	$\mu_1^f (mm^3)$ at final time $T = 500$	$\mu_1^{pd} (mm^3)$	E_{μ_1}
0.103	$7.67271875 \times 10^{-5}$	$7.67271872 \times 10^{-5}$	4.10×10^{-9}
0.15	$1.11701535 \times 10^{-4}$	$1.11701543 \times 10^{-4}$	7.97×10^{-8}
0.20	$1.48924575 \times 10^{-4}$	$1.48924641 \times 10^{-4}$	4.40×10^{-7}
0.3	$2.23420663 \times 10^{-4}$	$2.23420562 \times 10^{-4}$	4.53×10^{-7}
0.351	$2.61368442 \times 10^{-4}$	$2.61367974 \times 10^{-4}$	1.80×10^{-6}

Table 3. Comparison of the large time tumor mass and the predicted tumor mass for several values of a

373 3.2 Numerical simulations show how parameters influence equilibrium

374 The numerical methods were next used to assess how the parameters influence the equilibrium.
375 In particular, we wish to assess the evolution of the tumor mass at equilibrium according to
376 immune response and tumor growth parameters.

377 For the numerical simulations presented here, we thus work on the eigenproblem (6) and on
378 the constrained system (7)-(8). Unless precisely stated, the immune response parameters are
379 fixed to the lower bounds in **Table 1**. The tumor growth parameters are set to $a = 0.1 \text{ day}^{-1}$,
380 $V = 713.61 \mu m^3 \cdot \text{day}^{-1}$ and $R = 1.74 \times 10^{-7} \frac{\text{cell}_n \cdot \text{mm}^{-3}}{\text{cell}_n \cdot \mu m^3} \cdot \text{day}^{-1}$.

381 The main features of the solutions follow the observations made in (10), which were performed
382 with arbitrarily chosen values for the parameters. We observe that $\bar{\mu}_c(t) = \int_{\Omega} \delta(y) c(t, y) dy$
383 tends to the division rate a , which in this case corresponds to the leading eigenvalue of the cell-
384 division equation. It is important to note that the predicted diameter of the tumor at equilibrium
385 — see **Fig. 5** — is significantly below modern clinical PET scanners resolution limit, which
386 could detect tumors with a diameter larger than 7 mm (66). This is consistent with the standard
387 expectations about the equilibrium phase (3), but, of course, it makes difficult further comparison
388 of the prediction with data.

389 The aggressiveness of the tumor is characterized by the division rate, the variations of which
390 impact the size of the tumor at equilibrium: the larger a , the larger the residual tumor, see
391 **Fig. 6-(a)**. Increasing the immune strength A increases the efficacy of the immune response,
392 reducing the size of the residual tumor see **Fig. 6-(b)**. Similarly, increasing the mean rate of
393 influx of effector immune cells in the tumor microenvironment R , decreases the tumor size
394 at equilibrium, see **Fig. 6-(c)**. On the contrary, increasing the death rate of the immune cells
395 γ reduces the efficacy of the immune response and increases the equilibrium tumor size see
396 **Fig. 6-(d)**.

397 Moreover, as mentioned above, not only the parameters determine the equilibrium mass, but
398 they also impact how the equilibrium establishes. **Fig. 7-(a-c)** shows what happens by making
399 the tumor cell division rate a vary. There are more oscillations along time, with larger amplitude,
400 as a increases. Similar observations can be made when reducing the strength of the immune
401 system A (likely out of its realistic range), see **Fig 7-(d-f)**. The smaller A , the weaker the
402 damping of the oscillations and the longer the periods. We notice that the decay of the maximal
403 tumor radius holds at a polynomial rate. In extreme situations, either the damping is very
404 strong and the equilibrium establishes oscillation-free or the equilibrium does not establish on
405 reasonable observation times, and the evolution can be confounded with a periodic alternance of

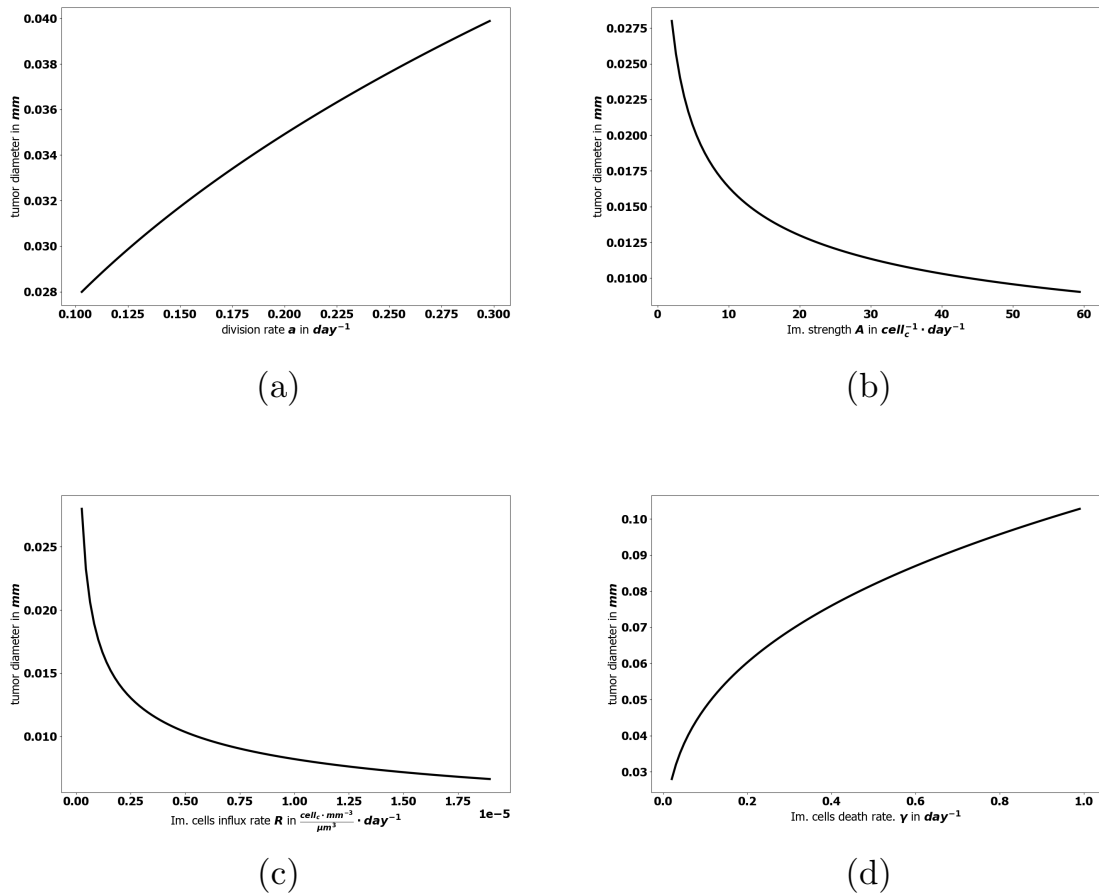


Figure 6. Evolution of the tumor diameter at equilibrium, with respect to **(a)**: the division rate of tumor cells a , **(b)**: the strength of the effector immune cells A , **(c)**: the influx rate of effector immune cells R , **(d)**: the natural death rate γ of the effector cells

406 growing and remission phases. Such scenario illustrates that the relevance of the equilibrium
 407 can be questionable depending on the value of the parameters. In what follows, we focus on the
 408 details of the equilibrium itself, rather than on the transient states.

409 **3.3 Global sensitivity analysis on the equilibrium mass identifies the key** 410 **parameters to target in cancer therapy**

411 Since the equilibrium state can be computed for a reduced numerical cost (it takes about 1/4
 412 of a second on a standard laptop), we can perform a large number of simulations, sampling
 413 the range of the parameters. This allows us to discuss in further details the influence of the
 414 parameters on the residual mass and, by means of a global sensitivity analysis, to make a
 415 hierarchy appear according to the influence of the parameters on this criterion. Ultimately, this
 416 study can help in proposing treatments that target the most influential parameters.

417 Details on the applied methods for the sensitivity analysis can be found in Appendix 2. Among
 418 the parameters, we distinguish:

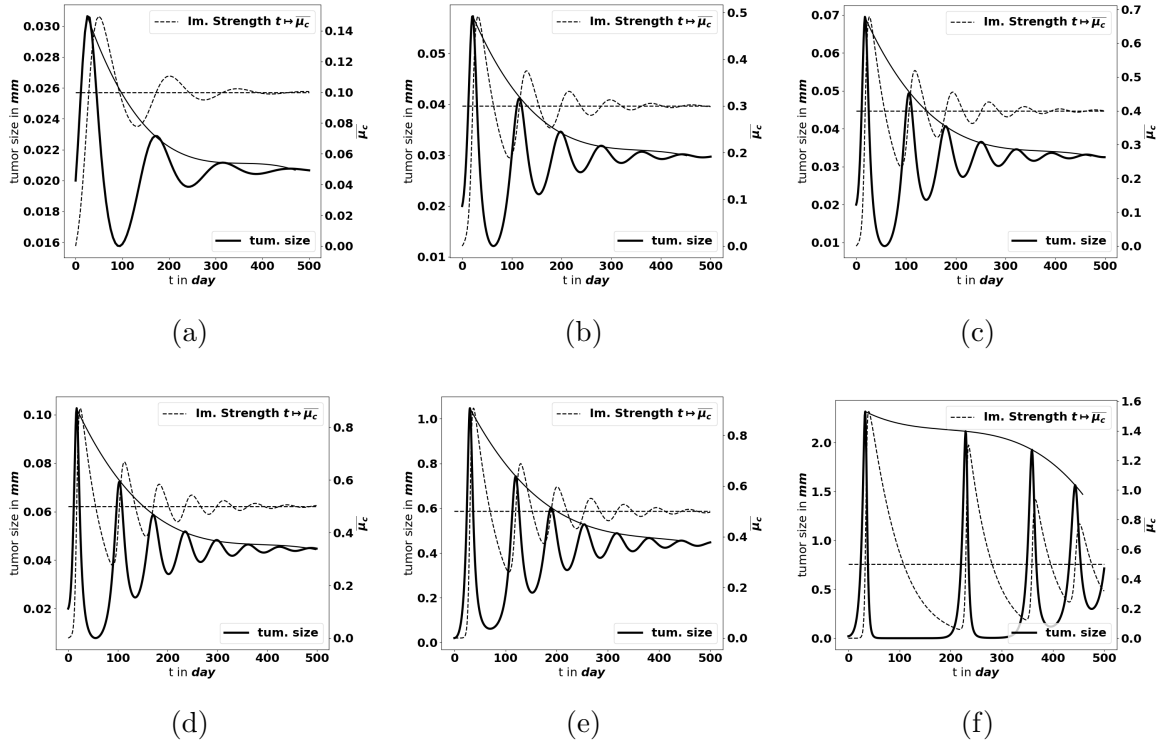


Figure 7. Large-time simulation of the PDE system: evolution of the tumor diameter (bold black line, left axis), and of the concentration of immune cells $\bar{\mu}_c$ (dotted grey line, right axis), for several values of the division rate a : **(a)**: $a = 0.1 \text{ day}^{-1}$, **(b)**: $a = 0.3 \text{ day}^{-1}$, **(c)**: $a = 0.4 \text{ day}^{-1}$ and for several values of the immune strength A : **(d)**: $A = 1 \text{ cell}^{-1} \cdot \text{day}^{-1}$, **(e)**: $A = 1 \cdot 10^{-3} \text{ cell}^{-1} \cdot \text{day}^{-1}$, **(f)**: $A = 1 \cdot 10^{-5} \text{ cell}^{-1} \cdot \text{day}^{-1}$. The horizontal dotted line represents the predicted asymptotic value for $\bar{\mu}_c$. The solid line gives the envelope of the oscillations, indicating a polynomial damping rate. The equilibrium needs more time to establish as the strength of the immune system decreases

- 419 •the tumor cell division rate a which drives the tumor aggressiveness,
420 •the efficacy of the immune system, governed by the mean influx rate of activated effector
421 immune cells R , the strength of the immune response A , the chemotactic sensitivity χ , the
422 death rate γ of the immune cells, and the strength of the chemical signal induced by each
423 tumor cell A_σ
424 •environmental parameters such as the diffusion coefficients D (for the immune cells) and \mathcal{K}
425 (for the chemokine concentration).

426 We assume that the input parameters except a and R are independent random variables. Due
427 to the lack of knowledge on the specific distribution of most of the parameters, the most suitable
428 probability distribution is the one which maximizes the continuous entropy ((67)), more precisely,
429 the uniform distribution over the ranges defined in **Table 1**. Therefore, the uncertainty in the
430 parameter values is represented by uniform distributions for the parameters $(A, \chi, D, A_\sigma, \gamma, \mathcal{K})$
431 and by log-normal distributions for the parameters a and R . In what follows, the total mass at
432 equilibrium, μ_1 , given by the power-dichotomy algorithm, is seen as a function of the uncertain

433 parameters:

$$\mu_1 = f(a, A, R, \chi, D, A_\sigma, \gamma, \mathcal{K}). \quad (15)$$

434 To measure how the total variance of the output μ_1 of the algorithm is influenced by some
435 subsets $i_1 \cdots i_p$ of the input parameters $i_1 \cdots i_k$ ($k \geq p$ being the number of uncertain input
436 parameters), we compute the so-called Sobol's sensitivity indices. The total effect of a specific
437 input parameter i is evaluated by the total sensitivity index $S_T^{(i)}$, the sum of the sensitivity
438 indices which contain the parameter i . (Details on the computed Sobol indices can be found
439 in Appendix 2.) The computation of these indices is usually based on a Monte Carlo (MC)
440 method (see (68, 69)) which requires a large number of evaluations of the model due to its slow
441 convergence rate ($O(1/\sqrt{N})$ where N is the size of the experimental sample). To reduce the
442 number of model evaluations, we use instead the so-called generalized Polynomial Chaos (gPC)
443 method (see (70)). The backbone of the method is based on building a surrogate of the original
444 model by decomposing the quantity of interest on a basis of orthonormal polynomials depending
445 on the distribution of the uncertain input parameters $\theta(\omega) = (a, A, R, \chi, D, A_\sigma, \gamma, \mathcal{K})$, where
446 ω represents an element of the set of possible outcomes. Further details on the method can be
447 found in (71). For uniform distributions, the most suitable orthonormal polynomial basis is the
448 Legendre polynomials. The analysis of the distribution of μ_1 after a suitable sampling of the
449 parameters space indicates that μ_1 follows a log-normal distribution. This distribution is not
450 uniquely determined by its moments (the Hamburger moment problem) and consequently cannot
451 be expanded in a gPC (see (72)). Based on this observation, to obtain a better convergence in
452 the mean square sense, we apply the gPC algorithm on the natural logarithm of the output μ_1 .
453 Typically, $\ln(\mu_1)$ is decomposed as follows:

$$\ln(\mu_1(\omega)) = \sum_{\alpha \in \mathcal{I}_{k,p}} q_\alpha L_\alpha(\theta(\omega)) + \varepsilon, \quad (16)$$

454 where ε corresponds to the approximation error, $\mathcal{I}_{k,p} = \{\alpha \in \mathbb{N}^k : \sum_{i=1}^k \alpha_i \leq p\}$ and p
455 represents the highest degree of the expansion. Hence, the dimension of the polynomial basis is
456 given by $\frac{(k+p)!}{k!p!}$. We reduce the number of model evaluations to 642 runs by constraining also
457 the parameters interaction order to 2. For our purpose, a degree $p = 5$ gives a better fit (see
458 **Fig. 8-a-b**) to the original model and the goodness of fit of the gPC algorithm is measured by a
459 Leave One Out Cross Validation (LOOCV) technique (73). The resulting LOO error indicates
460 0.4% prediction error. The Sobol's sensitivity indices are then computed from the exponential
461 of the surrogate model (16) by using Monte Carlo simulations combined with a careful space-
462 filling sampling of the parameters space (see (68, 74)). For the computations, a sample with
463 $N = 1.8 \times 10^6$ points has been used in order to get stable second order Sobol indices. Indeed,
464 the sensitivity indices that are needed to discriminate the impact of the input parameters are
465 the first and total Sobol' sensitivity indices. Here, the analysis revealed a significant difference
466 between some first order Sobol' indices and their corresponding total Sobol indices, which
467 indicated the importance of computing also the second order Sobol' indices.

468 It is important to stress that the obtained results, and the associated conclusions, could be
469 highly dependent on the range of the parameter values. This observation makes the measurement
470 / estimation of the parameters a crucial issue which can be dependent on the type of cancer

471 analyzed.

472

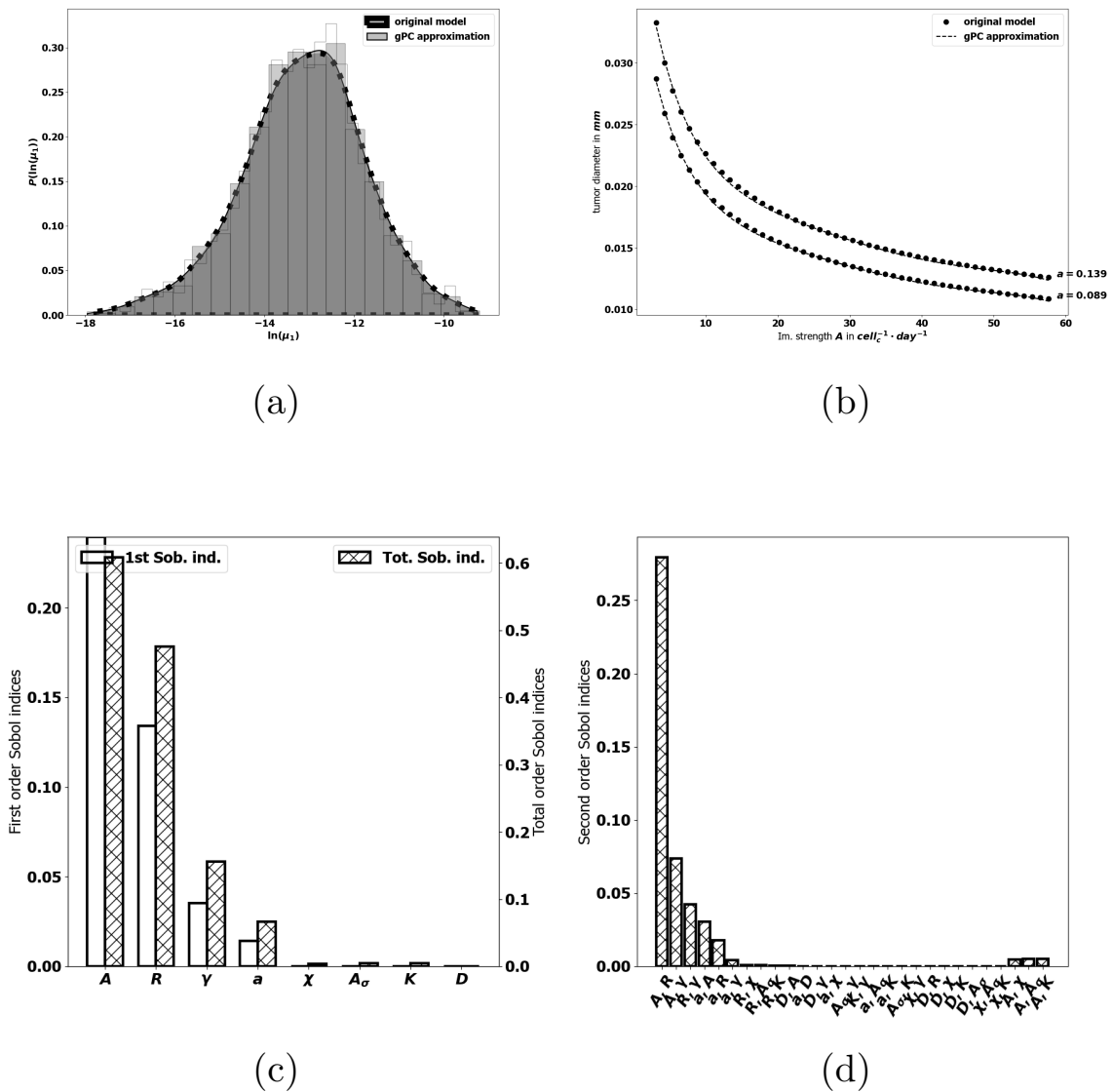


Figure 8. (a): comparison between the pdf of $\ln(\mu_1)$ from the gPC approximation and the pdf from the original model. (b): Comparison between the value of μ_1 generated by the power-dichotomy algorithm and the gPC approximation. (c): First (empty, left scale) and total (dashed, right scale) order Sobol indices for μ_1 . (d) Second order Sobol indices for μ_1

473 **Efficacy of the immune response.** The first order Sobol indices represented in **Fig. 8-c** indicate
 474 that the parameters which impact the most the variability of the immune-controlled tumor mass
 475 at equilibrium are:

- 476 •the strength of the lethal action of the immune cells on the tumor cells A , by far the most
 477 influential,

478 and three additional parameters

- 479 •the influx rate of activated effector immune cells into the tumor microenvironment R .
- 480 •the natural death rate γ of the effector immune cells,
- 481 •and the division rate a of the tumor cells.

482 This result is consistent with the observations made from the numerical experiments above and
483 in (10), showing a prominent role of the immune response which can be enhanced by increasing
484 either A or R , and decreasing γ . That A is the most influential parameter is not that surprising but
485 it is remarkable how far its importance exceeds that of the other parameters. It is also puzzling
486 to see that the chemotactic sensitivity χ , like the strength of the chemical signal induced by each
487 tumor cell A_σ , the space diffusion coefficient of the effector immune cells D and the diffusion
488 coefficient of the chemokines \mathcal{K} , have a negligible influence on the immune-controlled tumor
489 mass, see **Fig. 8-c**, whether individually or in combination with other parameters. This result is
490 consistent with the necessity for immune cells to be able to effectively kill the tumor cells once
491 they reach the tumor site. The second order Sobol' indices indicate that the leading interactions
492 are the pairs (A, R) , (A, γ) , (R, γ) , (a, A) , (a, R) and (a, γ) . Accordingly, in order to enhance
493 the immune response, an efficient strategy can be to act simultaneously on the immune strength
494 A together with the influx rate of activated immune effector cells R . Increasing such influx into
495 the tumor microenvironment by enhancing the activation/recruitment processes leading to the
496 conversion of naive immune cells into activated immune cells potentiate anti-tumor immune
497 responses. Besides, the natural death rate γ of the effector immune cells combined to A and R
498 have an impact, as well as A combined with the division rate of the tumor cells, a .
499

500 **The tumor aggressiveness.** The tumor aggressiveness is mainly described by the cell division
501 rate a . The first order Sobol indice indicates that a influences significantly the tumor mass at
502 equilibrium, and we observe that the total Sobol index of a is higher than the individual one.
503 This indicates that this parameter has strong interactions with the others. By taking a look at
504 **Fig. 8-d** we remark that a interacts significantly with the parameters A, R, γ . However, the
505 most significant interaction is the one with A . This suggests that combining therapies targeting
506 tumor and immune cells should be more efficient at maintaining immune-mediated tumor mass
507 dormancy (75).
508

509 **Towards optimized treatments.** Because equilibrium state can be computed for a reduced
510 numerical cost, it allows a large number of simulation to be performed in a minimal time, so
511 that an extensive sampling of the range of the parameters can be tested. The flexibility of the
512 numerical simulations provides valuable tools to assess the efficiency of a variety of therapeutic
513 strategies and select those that sustain a viable equilibrium and prevent cancer relapses after a
514 surgery or a treatment. **Fig. 9** illustrates how the equilibrium mass is impacted when combining
515 variations of two parameters, namely the immune strength A combined to the tumor cell division
516 rate a , the mean rate of influx of effector immune cells R or the death rate of effector immune
517 cells γ ; and the tumor cell division rate a with the death rate γ . Interestingly, a reduction of the
518 tumor mass at equilibrium can be obtained significantly more easily by acting on two parameters
519 than on a single one. For instance, reducing the tumor cell division rate a from 0.35 to 0.1 cannot

520 reduce the diameter of the tumor below .025 mm, with $A = 1$; while the final size is always
 521 smaller when $A = 3.95$. This observation highlights the interest of combined treatments having
 522 such complementary actions. The interest is two-fold: either smaller residual tumors can be
 523 obtained by pairing two actions, or the same final tumor size can be obtained with a combined
 524 treatment having less toxicity than a mono-therapy.

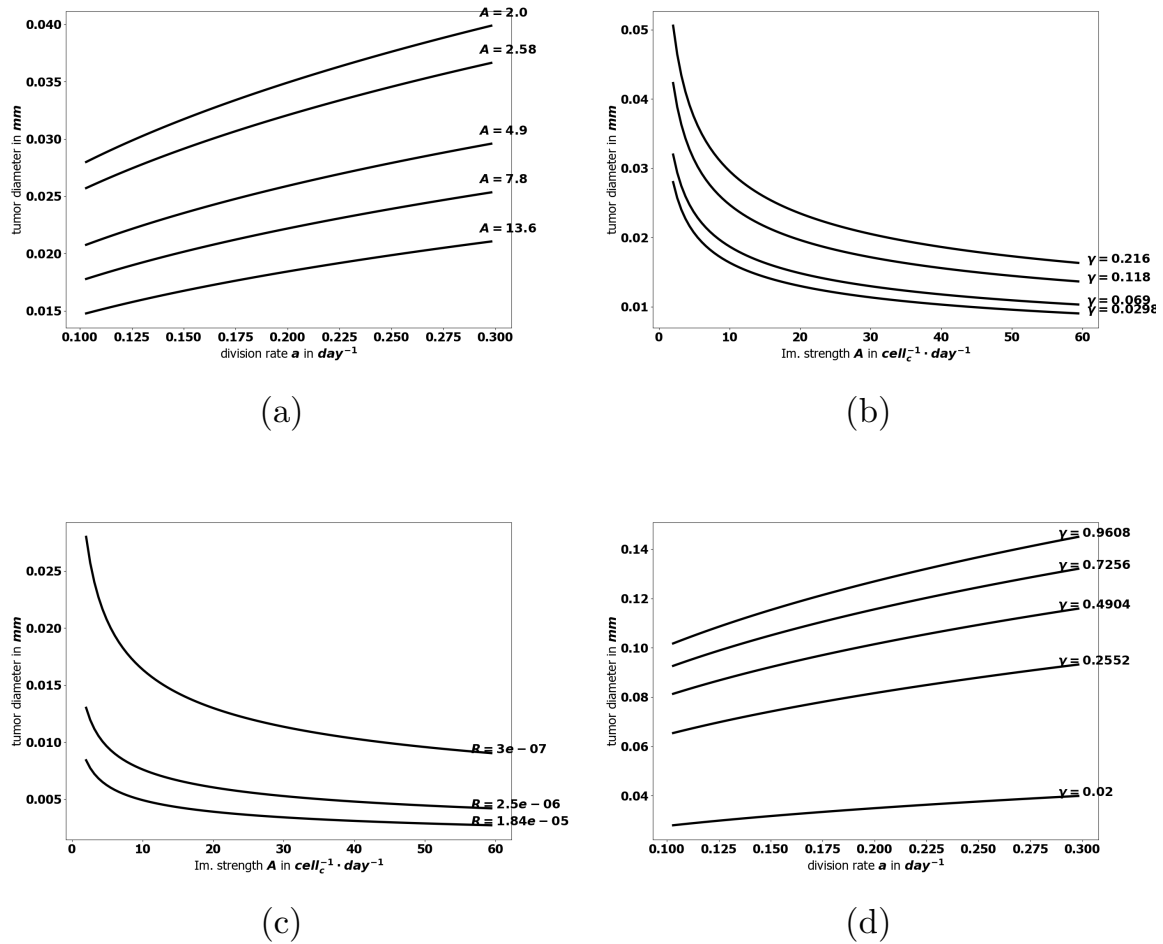


Figure 9. Evolution of the tumor diameter at equilibrium, (a): with respect to the division rate a for several values of the immune strength A , (b): with respect to the immune strength A for several values of the death rate γ , (c): with respect to the immune strength A for several values of the influx rate of effector immune cells R , and (d): with respect to the division rate a for several values of the death rate γ .

4 DISCUSSION

525 Controlling parameters that maintain immune-mediated tumor mass dormancy is key to the
 526 successful development of future cancer therapies. To understand how equilibrium establishes
 527 and how it is influenced by immune, environmental and tumor-related parameters, we evaluate
 528 the tumor mass which tends to a constant at equilibrium. In this study, we make use of the
 529 space and size structured mathematical model developed in (10) to provide innovative, efficient

530 methods to predict, at low numerical cost, the residual tumor mass at equilibrium. By means
531 of numerical simulations and global sensitivity analysis, we identify the elimination rate A
532 of tumor cells by immune cells as the most influential factor. Therefore, the most efficient
533 therapeutic strategy is to act primarily on the immune system rather than on the tumor itself.
534 We also demonstrate the need to develop combined cancer treatments, boosting the immune
535 capacity to kill tumor cells (increase A), the conversion into efficient immune cells (increase
536 R), reducing natural death rate of effector immune cells (decrease γ) and reducing the ability of
537 tumor cells to divide (decrease a). The combination of such approaches definitely outperforms
538 the performances of a single action; it permits to maintain the tumor in a long-lasting equilibrium
539 state, far below measurement capabilities.

540 Generally, therapeutic strategies are designed to target preformed, macroscopic cancers.
541 Indeed, patients are diagnosed once their tumor is established and measurable, thus at the
542 escape phase of the cancer immunoediting process (1). The goal of successful treatments is
543 to revert to the equilibrium phase and ultimately to tumor elimination. Experimental evidence
544 and clinical observations indicate that such equilibrium exists but it is difficult to study and
545 measure, the residual tumor mass being below detection limits (1, 2, 3). It is regarded as “a
546 immune-mediated tumor mass dormancy” when the rate of cancer cell proliferation matches
547 their rate of elimination by immune cells. In human, cancer recurrence after therapy and long
548 periods of remission or detection of low number of tumor cells in remission phases are suggestive
549 of such equilibrium phase. Mathematical models can also be used to provide evidence of such
550 state. The system of partial differential equations proposed in (10) is precisely intended to
551 describe the earliest stages of immune control of tumor growth. Remarkably, while being in
552 the most favorable condition, only taking into account the cytotoxic effector immune cells and
553 no immunosuppressive mechanisms, the model reproduces the formation of an equilibrium
554 phase with maintenance of residual tumor cells rather than their complete elimination. Besides
555 suggesting that elimination may be difficult to reach, this finding also brings out the role of
556 leading parameters that shape the equilibrium features and opens new perspectives to elaborate
557 cancer therapy strategies that reach this state of equilibrium.

558 To decipher tumor-immune system dynamics leading to equilibrium state, we have developed
559 here computational tools. The total mass of the tumor is a critical criterion of the equilibrium and
560 was used to predict parameters that contribute the most to the establishment of the equilibrium.
561 By means of global sensitivity analysis, we identified one leading parameter, A , and three
562 others, R , γ and a that affect the most the variability of the immune-controlled tumor mass;
563 A , R and γ are related to immune cells, and a to tumor cells. Moreover, the influence of the
564 leading parameters is significantly increased when they are paired. This observation supports
565 the development of combined therapeutic treatments which would be more efficient at reducing
566 tumor growth and toxicity. Because the pairs (A, R) , (A, γ) , (R, γ) , (A, a) , (a, R) and (a, γ)
567 are the most influential, we predict that a combination of drugs enhancing antitumor immune
568 responses with drugs diminishing tumor aggressiveness will be the most efficient. This is
569 consistent with the clinical benefit obtained when chemotherapies reducing the tumor cell
570 division rate a are combined with immunotherapies increasing A and R , (75). The parameter A
571 which governs the efficacy of the immune system to eliminate tumor cells, is the most influential.
572 This finding is consistent with the observation that “hot” tumors infiltrated with immune cells

573 have better prognostic than “cold” tumors (76) and that the immune cells with the strongest
574 positive impact on patient’s survival are the cytotoxic CD8⁺ T cells (77). It is also in line with the
575 success of ICP which revert immune tolerance triggered by chronic activation and upregulation
576 of exhaustion markers on effector T and NK cells, thus not only increasing the parameter A
577 but also R (78). The leading role of the parameter A is also demonstrated by experimental
578 studies and clinical trials, such as adoptive transfer of CAR-T and CAR-NK cells engineered to
579 attack cancer cells, immunomodulating antibody therapies or cancer vaccines which boost the
580 antitumor immune response (75, 79, 80, 81). Finally, our finding that the parameter γ is highly
581 influential is confirmed by the administration of cytokines that stimulate and increase effector
582 T and NK cell survival which are efficient at controlling tumor growth (81). Thus, altogether,
583 these experimental and clinical data validate the numerical method.

584 Interestingly, besides the dominant role of the parameter A , only two additional parameters
585 related to immune cells R, γ seem to have an influence on the tumor mass at equilibrium. These
586 data predict that to enhance the immune response, it is more efficient to increase the rate of influx
587 and conversion of naive immune cells into effector cells (parameter R) or to increase the lifespan
588 of immune effectors (parameter γ) than to increase chemotaxis as a whole (parameters $\chi, A_\sigma,$
589 \mathcal{K}). The lack of influence of chemotaxis emphasizes that the localization of immune cells within
590 tumors is necessary but not sufficient. Indeed, the leading influence of the parameters A, R, γ
591 stresses the importance of having functional immune cells infiltrating tumors. Overcoming
592 immune suppression is therefore highly relevant in therapeutic strategies.

593 Targeting Immune-mediated tumor mass dormancy is gaining more and more attention, having
594 been linked to recurrence and metastasis (9, 82). The persistence of undetectable tumor cells
595 after primary tumor resection at the primary site but also their spreading to metastatic niches
596 are major causes of treatment failure. Thus, developing strategies to maintain an equilibrium
597 between these tumor cells and the immune response is crucial. Interestingly, a recent study
598 demonstrated a role of the NK cell reservoir in blocking the reawakening of dormant tumor cells
599 (83). The mechanisms involve IL-15 that drives NK cell proliferation and IFN- γ secreted by NK.
600 Therapies boosting NK cell activity like IL-15 superagonists, or engineered NK cell engagers
601 are therefore promising strategies to sustain NK cell-mediated maintenance of tumor dormancy
602 (83, 84).

603 It is appropriate to finally comment on the limitations of this work and provide new avenues
604 for future research. Firstly, the analysis focuses on the asymptotic state, taking full advantage of
605 its mathematical interpretation which makes it easily computable. However, the transient states
606 and the rate at which the equilibrium becomes observable are simply disregarded, while they are
607 certainly essential for assessing the biological relevance of the equilibrium state. Further analysis
608 is therefore needed in order to understand how the parameters of the model influence the trend to
609 equilibrium. Secondly, the modeling approach is facing contradictory requests: on the one hand,
610 the lack of knowledge on the parameters motivates working with a reduced set of equations,
611 at the cost of considering an “averaged” behavior (say for instance between different types
612 of immune cells); on the other hand, it might be important to keep under consideration many
613 relevant and competing effects of cellular interactions. These issues can be addressed with a
614 better access to biological data and through the development of dedicated methods of parameter
615 identification. This is of course even more important when describing the effects of treatments.

616 Thirdly, the present analysis is limited to an idealized situation in which many important effects
617 have been overlooked. In particular, the immune response can also promote the tumor growth.
618 Considering such immune actions leads to a much more complex dynamical behavior and the
619 possible establishment of an escape phase, as shown in (42). Finally geometrical aspects and
620 heterogeneity are poorly addressed and restrict the relevance of the description to the earliest
621 stages of the tumor development. More complex models, with a full space structuration, should
622 be elaborated in order to obtain a more accurate description of the tumor microenvironment.

5 CONCLUSION

623 In conclusion, clinical trials have been undertaken quite often on assumptions from acquired
624 knowledge on tumor development and immune responses to cancer cells, but without tools to
625 help the decision-making. The numerical methods developed here provide valuable hints for the
626 design and the optimization of antitumor therapies. The approach is in agreement with published
627 experimental findings and clinical evidence. By adapting the range of the parameters to the
628 biological values, one can more precisely adapt the therapeutic strategies to specific types of
629 tumors. We thus conclude that mathematical modelling combined with numerical validation
630 provide valuable information that could contribute to better stratify the patients eligible for
631 treatments and consequently save time and lives. In addition, it could also help to decrease the
632 burden of treatment cost providing hints on optimized therapeutic strategies.

CONFLICT OF INTEREST STATEMENT

633 The authors declare that the research was conducted in the absence of any commercial or
634 financial relationships that could be construed as a potential conflict of interest.

AUTHOR CONTRIBUTIONS

635 Conception and design: K. A., V. M. B., T. G.; Development of methodology: K. A., V. M.
636 B., T. G.; Acquisition of data (provided animals, acquired and managed patients, provided
637 facilities, etc.): F. A., V. M. B., S. K.; Analysis and interpretation of data (e.g., statistical analysis,
638 biostatistics, computational analysis): K. A., V. M. B., T. G.; Writing, review, and/or revision of
639 the manuscript: K. A., F. A., V. M. B., T. G.; Study supervision: F. A., V. M. B., T. G.;

FUNDING

640 This work was supported by the French Government (National Research Agency, ANR) through
641 the “Investments for the Future” programs LABEX SIGNALIFE ANR-11-LABX-0028 and
642 IDEX UCAJedi ANR-15-IDEX-01.

ACKNOWLEDGMENTS

643 The authors acknowledge the support of UCAnCer, an incentive Université Côte d’Azur network,
644 which has permitted and encouraged this collaboration. We thank the IPMC’s animal house and
645 Imaging/Flow cytometry core facilities for technical support.

DATA AVAILABILITY STATEMENT

646 Numerical data necessary to replicate the results of the paper, as well as the codes used to
647 produce the results, are available at the URL [https://github.com/atsoukevin93/
648 tumorgrowth](https://github.com/atsoukevin93/tumorgrowth).

1 COMPUTATION OF THE EIGEN-ELEMENTS OF THE GROWTH-DIVISION EQUATION

649 The binary division operator (2) is a very specific case, and for applications it is relevant to deal
650 with more general expressions. Namely, we have

$$Q(n)(t, z) = -a(z)n(t, z) + \int_z^\infty a(z')k(z|z')n(t, z') dz'. \quad (17)$$

651 In (17), $a(z')$ is the frequency of division of cells having size z' , and $k(z|z')$ gives the size-
652 distribution that results from the division of a tumor cell with size z' . What is crucial for
653 modeling purposes is the requirement

$$\int_0^z z'k(z'|z) dz' = z,$$

654 which is related to the principle that cell-division does not change the total mass

$$\int_0^\infty zQ(n) dz = 0.$$

655 We refer the reader to (32) for examples of such cell-division operators and the analysis of the
656 eigenvalue problem (6) under quite general assumptions of the growth rate V , the frequency a
657 and the kernel k . Our numerical method can handle such general coefficients.
658

659 It is important to bear in mind the main arguments of the proof of the existence-uniqueness of
660 the eigenpair (λ, \bar{N}) for the growth-division equation. Namely, for Λ large enough we consider
661 the *shifted* operator

$$\mathcal{T}_\Lambda N = \Lambda N + \partial_z(VN) + aN - \int_z^\infty a(z')k(z|z')N(z') dz'.$$

662 Then, we check that the operator \mathcal{S}_Λ which associates to a function f the solution n of
663 $\mathcal{T}_\Lambda n = f$ fulfills the requirements of the Krein-Rutman theorem (roughly speaking, positivity
664 and compactness), see (85). Accordingly, the quantity of interest λ is related to the leading
665 eigenvalue of \mathcal{S}_Λ . In fact, this reasoning should be applied to a somehow truncated and
666 regularized version of the operator, and the conclusion needs further compactness arguments;
667 nevertheless this is the essence of the proof. In terms of numerical method, this suggests to
668 appeal to the inverse power algorithm, applied to a discretized version of the equation. However,
669 we need to define appropriately the shift parameter Λ . As far as the continuous problem is
670 considered, Λ can be estimated by the parameters of the model (32), but it is critical for practical

671 issues to check whether or not this condition is impacted by the discretization procedure. This
672 information will be used to apply the inverse power method to the discretized and shifted version
673 of the problem.

674 1.1 Analysis of the discrete problem

675 The computational domain for the size variable is the interval $[0, R]$ where R is chosen large
676 enough: due to the division processes, we expect that the support of the solution remains
677 essentially on a bounded interval, and the cut-off should not perturb too much the solution. In
678 what follows, the size step $h = z_{i+1} - z_i$ is assumed to be constant. The discrete unknowns N_i ,
679 with $i \in \{1, \dots, I\}$ and $h = R/I$, are intended to approximate $N(z_i)$ where $z_i = ih$. The integral
680 that defines the gain term of the division operator is approximated by a simple quadrature rule.
681 For the operator (2) the kernel involves Dirac masses which can be approached by peaked
682 Gaussian. We introduce the operator $\mathcal{T}_\Lambda^h : \mathbb{R}^I \rightarrow \mathbb{R}^I$ defined by

$$\begin{cases} (\mathcal{T}_\Lambda^h N)_i = F_i - F_{i-1} + h(\Lambda + a_i)N_i \\ \quad - h^2 \sum_{j=i}^I a(z_j)k(z_i|z_j)N_j, \\ N_1 = 0 \end{cases} \quad (18)$$

683 where $F_i = V_{i+1/2}N_i$ represents the convective numerical flux on the grid point $z_{i+1/2} =$
684 $(i + 1/2)h$, $i \in \{1, \dots, I\}$. This definition takes into account that the growth rate is non negative,
685 and applies the upwinding principles. Note that the step size h should be small enough to capture
686 the division of small cells, if any. The following statement provides the a priori estimate which
687 allows us to determine the shift for the discrete problem.

688 **THEOREM 1.1.** *We suppose that*

689 *i) $z \mapsto V(z)$ is a continuous function which lies in L^∞ and it is bounded from below by a positive*
690 *constant,*

691 *ii) $h \sum_{j=1}^I a(z_j)k(z_i|z_j)$ remains bounded uniformly with respect to h ,*

692 *iii) for any $i \in \{1, \dots, I - 1\}$, there exists $j \in \{i + 1, \dots, I\}$ such that $a(z_j)k(z_i|z_j) > 0$,*

693 *iv) there exists $Z_0 \in (0, \infty)$ such that, setting $\bar{N}(z) = h \sum_{j=2}^I k(z_j|z)$, we have $a(z)(\bar{N}(z) -$
694 $1) \geq \nu_0 > 0$ for any $z \geq Z_0$.*

695 *Let*

$$\Lambda > \frac{\|V\|_{L^\infty}}{\min_{j \in \{1, \dots, I\}} |V_{j+1/2}|} \max_{k \in \{1, \dots, I\}} \left(h \sum_{j=k}^I a_j k(z_k|z_j) \right) - \min_{j \in \{1, \dots, I\}} |a_j|, \quad (19)$$

696 *and we suppose that $R > Z_0$ is large enough. Then, \mathcal{T}_Λ^h is invertible and there exists a pair*
697 *$\mu > 0$, $N \in \mathbb{R}^I$ with positive components, such that $\text{Ker}((\mathcal{T}_\Lambda^h)^{-1} - \mu) = \text{Span}\{N\}$. Moreover*
698 *$\lambda = \Lambda - \frac{1}{\mu} > 0$.*

699 Note that the sum that defines $\bar{N}(z)$ is actually reduced over the indices such that $jh \leq z$; this
700 quantity is interpreted as the expected number of cells produced from the division of a cell with
701 size z so that the fourth assumption is quite natural.

702 PROOF. Let $f \in \mathbb{R}^I$. We consider the equation

$$\mathcal{T}_\Lambda^h N = f.$$

703 We denote $N = \mathcal{S}_\Lambda^h f$ the solution. We are going to show that \mathcal{S}_Λ^h is well defined and satisfies
704 the assumptions of the Perron-Frobenius theorem, see e. g. (47, Theorem 1.37 & Corollary 1.39)
705 or (86, Chapter 5).

706 It is convenient to introduce the change of unknown $U_i = N_i V_{i+1/2}$, $\forall i \in \{1, \dots, I\}$. The
707 problem recasts as

$$\left\{ \begin{array}{l} (\widetilde{\mathcal{T}}_\Lambda^h U)_i = h \frac{f_i}{V_{i+1/2}}, \text{ with} \\ (\widetilde{\mathcal{T}}_\Lambda^h U)_i = U_i - U_{i-1} + h \frac{\Lambda + a_i}{V_{i+1/2}} U_i \\ \quad - h^2 \sum_{j=i}^I \frac{a_j}{V_{j+1/2}} k(z_i | z_j) U_j, \\ U_1 = 0. \end{array} \right. \quad (20)$$

The solution is interpreted as the fixed point of the mapping

$$\xi \mapsto U = A^h \xi$$

where U is given by $U_1 = 0$ and

$$U_i = U_{i-1} + h^2 \sum_{j=i}^I \frac{a_j}{V_{j+1/2}} k(z_i | z_j) \xi_j + h \frac{f_i}{V_{i+1/2}}.$$

We are going to show that A^h is a contraction: $\|A^h \xi\|_{\ell^\infty} \leq k \|\xi\|_{\ell^\infty}$ for some $k < 1$. Multiplying
(20) by $\text{sign}(U_i)$, we obtain

$$\begin{aligned} & \left(1 + h \frac{\Lambda + a_i}{V_i}\right) \text{sign}(U_i) U_i = \left(1 + h \frac{\Lambda + a_i}{V_i}\right) |U_i| \\ & = \text{sign}(U_i) U_{i-1} + h^2 \sum_{j=i}^I \frac{a_j}{V_{j+1/2}} k(z_i | z_j) \text{sign}(U_i) \xi_j \\ & \leq |U_{i-1}| + h^2 \sum_{j=i}^I \frac{a_j}{V_{j+1/2}} k(z_i | z_j) |\xi_j|. \end{aligned}$$

708 We multiply this by the weight $\prod_{l=1}^{i-1} \left[1 + h \frac{\Lambda + a_l}{V_{l+1/2}}\right]$, where all factors are ≥ 1 . We get

$$\begin{aligned} & |U_i| \prod_{l=1}^i \left[1 + h \frac{\Lambda + a_l}{V_{l+1/2}}\right] \\ & \leq |U_{i-1}| \prod_{l=1}^{i-1} \left[1 + h \frac{\Lambda + a_l}{V_{l+1/2}}\right] \\ & \quad + h^2 \prod_{l=1}^i \left[1 + h \frac{\Lambda + a_l}{V_{l+1/2}}\right] \sum_{j=i}^I \frac{a_j}{V_{j+1/2}} k(z_i|z_j) |\xi_j|. \end{aligned}$$

709 Then, summing over $i \in \{2, \dots, m\}$ yields

$$\begin{aligned} & |U_m| \prod_{l=1}^m \left[1 + h \frac{\Lambda + a_l}{V_{l+1/2}}\right] \\ & \leq |U_1| \left[1 + h \frac{\Lambda + a_1}{V_{3/2}}\right] \\ & \quad + h^2 \sum_{i=2}^m \prod_{l=1}^i \left[1 + h \frac{\Lambda + a_l}{V_{l+1/2}}\right] \sum_{j=i}^I \frac{a_j}{V_{j+1/2}} k(z_i|z_j) |\xi_j| \end{aligned}$$

710 where actually $U_1 = 0$. It follows that

$$\begin{aligned} |U_m| & \leq h^2 \sum_{i=2}^m \prod_{l=i}^m \left[1 + h \frac{\Lambda + a_l}{V_{l+1/2}}\right]^{-1} \sum_{j=i}^I \frac{a_j}{V_{j+1/2}} k(z_i|z_j) |\xi_j| \\ & \leq \frac{h^2 \|\xi\|_{\ell^\infty}}{\min_{j \in \{1, \dots, I\}} V_{j+1/2}} \sum_{i=2}^m \prod_{l=i}^m \left[1 + h \frac{\Lambda + a_l}{V_{l+1/2}}\right]^{-1} \sum_{j=i}^I a_j k(z_i|z_j) \\ & \leq \frac{h^2 \|\xi\|_{\ell^\infty}}{\min_{j \in \{1, \dots, I\}} V_{j+1/2}} \left\| \sum_{j=i}^I a_j k(z_i|z_j) \right\|_{\ell^\infty} \\ & \quad \sum_{i=2}^m \left[1 + h \frac{\Lambda + \min_{l \in \{1, \dots, I\}} a_l}{\|V\|_{L^\infty}}\right]^{i-m+1} \\ & \leq \frac{h \|\xi\|_{\ell^\infty}}{\min_{j \in \{1, \dots, I\}} V_{j+1/2}} \left\| \sum_{j=i}^I a_j k(z_i|z_j) \right\|_{\ell^\infty} \\ & \quad \left[\frac{\Lambda + \min_{l \in \{1, \dots, I\}} a_l}{\|V\|_{L^\infty}} \right]^{-1}. \end{aligned}$$

711 Therefore, A^h is a contraction provided (19) holds. This estimate is similar to the condition
712 obtained for the continuous problem, see (32, Proof of Theorem 2, Appendix B); the
713 discretization does not introduce further constraints.

714 We are now going to show that \mathcal{T}_Λ^h is a M -matrix when (19) holds. Let $f \in \mathbb{R}^I \setminus \{0\}$ with
715 non negative components. Let $U \in \mathbb{R}^I$ satisfy $(\widetilde{\mathcal{T}}_\Lambda^h U)_i = h \frac{f_i}{V_{i+1/2}}$. Let i_0 be the index such that
716 $U_{i_0} = \min \{U_i, i \in \{2, \dots, I\}\}$. We have

$$\begin{aligned} & U_{i_0} \left(1 + h \frac{\Lambda + a_{i_0}}{V_{i_0+1/2}} \right) \\ &= U_{i_0-1} + h^2 \sum_{j=i_0}^I \frac{a_j}{V_{j+1/2}} k(z_{i_0}|z_j) U_j + h \frac{f_{i_0}}{V_{i_0+1/2}} \\ &\geq U_{i_0} \left(1 + h^2 \sum_{j=i_0}^I \frac{a_j}{V_{j+1/2}} k(z_{i_0}|z_j) \right) + h \frac{f_{i_0}}{V_{i_0+1/2}}. \end{aligned} \quad (21)$$

717 Since $f_{i_0} \geq 0$, we get

$$U_{i_0} \underbrace{\left(\frac{\Lambda + a_{i_0}}{V_{i_0+1/2}} - h \sum_{j=i_0}^I \frac{a_j}{V_{j+1/2}} k(z_{i_0}|z_j) \right)}_{>0 \text{ by (19)}} \geq 0,$$

718 which tells us that $U_{i_0} \geq 0$. Suppose $U_{i_0} = 0$ for some $i_0 > 1$. Coming back to (21), we deduce
719 that U_{i_0-1} vanishes too, and so on and so forth, we obtain $U_1 = \dots = U_{i_0} = 0$. Finally, we use
720 the irreducibility assumption iii): we can find $j_0 > i_0$ such that $\frac{a_{j_0}}{V_{j_0+1/2}} k(z_{i_0}|z_{j_0}) > 0$ and (21)
721 implies $\frac{a_{j_0}}{V_{j_0+1/2}} k(z_{i_0}|z_{j_0}) U_{j_0} = 0$, so that $U_{j_0} = 0$. We deduce that $U = 0$, which contradicts
722 $f \neq 0$. Therefore the components of U are positive, but U_1 .

We conclude by applying the Perron-Froebenius theorem to $(\mathcal{T}_\Lambda^h)^{-1}$, (86, Chapter 5). It remains to prove that $\lambda = \Lambda - \frac{1}{\mu}$ is positive, with μ the spectral radius of $(\mathcal{T}_\Lambda^h)^{-1}$. To this end, we make use of assumption iv). We set $Z_0 = i_0 h$. We argue by contradiction, supposing that $\lambda = \Lambda - 1/\mu < 0$. We consider the eigenvector with positive components and normalized by the condition $h \sum_{i=1}^I U_i = 1$. We have

$$\begin{aligned} (\widetilde{\mathcal{T}}_0^h U)_i &= U_i - U_{i-1} + \frac{a_i}{V_{i+1/2}} h U_i \\ &\quad - h^2 \sum_{j=i}^I \frac{a_j}{V_{j+1/2}} k(z_i|z_j) U_j = -\lambda U_i \geq 0. \end{aligned}$$

It follows that, for $m \geq i_0$,

$$\begin{aligned}
U_m &\geq -h \sum_{i=2}^m \frac{a_i}{V_{i+1/2}} U_i + h^2 \sum_{i=2}^m \sum_{j=i}^I \frac{a_j}{V_{j+1/2}} k(z_i|z_j) U_j \\
&\geq -h \sum_{i=2}^m \frac{a_i}{V_{i+1/2}} U_i + h \sum_{j=2}^m \left(h \sum_{i=2}^j k(z_i|z_j) \right) \frac{a_j}{V_{j+1/2}} U_j \\
&\geq -h \sum_{i=2}^m \frac{a_i}{V_{i+1/2}} U_i + h \sum_{j=2}^m \bar{\mathcal{N}}(z_j) \frac{a_j}{V_{j+1/2}} U_j \\
&\geq h \sum_{i=2}^m (\bar{\mathcal{N}}(z_i) - 1) \frac{a_i}{V_{i+1/2}} U_i \\
&\geq h \sum_{i=i_0}^m (\bar{\mathcal{N}}(z_i) - 1) \frac{a_i}{V_{i+1/2}} U_i \geq \frac{\nu_0}{\|V\|_{L^\infty}} h \sum_{i=i_0}^m U_i.
\end{aligned}$$

723 It implies

$$1 = h \sum_{m=1}^I U_m \geq h \sum_{m=i_0}^I U_m \geq h(I - i_0) \frac{\nu_0}{\|V\|_{L^\infty}} h \sum_{i=i_0}^m U_i.$$

724 We arrive at

$$1 \geq (R - Z_0) \frac{\nu_0}{\|V\|_{L^\infty}},$$

725 a contradiction when R is chosen large enough (but how large R should be does not depend on
726 h). Therefore, we conclude that $\lambda > 0$.

727 1.2 Numerical approximation of (λ, N)

728 We compute (an approximation of) the eigenpair (λ, N) by using the inverse power method
729 which finds the eigenvalue of $(\mathcal{T}_\Lambda^h)^{-1}$ with largest modulus:

730 • We pick Λ verifying (19).

731 • We compute once for all the LU decomposition of the matrix \mathcal{T}_Λ^h .

732 • We choose a threshold $0 < \epsilon \ll 1$.

733 • We start from a random vector $N^{(0)}$ and we construct the iterations

734 • $LUq^{(k+1)} = N^{(k)}$,

735 • $N^{(k+1)} = \frac{q^{(k+1)}}{\|q^{(k+1)}\|}$

736 until the relative error $\frac{\|N^{(k+1)} - N^{(k)}\|}{\|N^{(k)}\|} \leq \epsilon$ is small enough. Then, given the last iterate $N^{(K)}$,

737 we set $LUq = N^{(K)}$, $\tilde{\mu} = \frac{q \cdot N^{(K)}}{N^{(K)} \cdot N^{(K)}}$, and $\tilde{\lambda} = \Lambda - 1/\tilde{\mu}$.

738 This approach relies on the ability to approximate correctly the eigenpair of the growth-
739 fragmentation operator. In particular, it is important to preserve the algebraic multiplicity.

740 This issue is quite subtle and it is known that the pointwise convergence of the operator is not
741 enough to guarantee the convergence of the eigenelements and the consistency of the invariant
742 subspaces, see (48) for relevant examples. This question has been thoroughly investigated in

743 (48, 49) which introduced a suitable notion of stability. It turns out that one needs a uniform
744 convergence of the operators. Namely, here, we should check that $\|(\mathcal{T}_\Lambda^I)^{-1} - (\mathcal{T}_\Lambda)^{-1}\| \rightarrow 0$
745 as $I \rightarrow \infty$. In the present framework, a difficulty relies on the fact that the size variable lies in
746 an unbounded domain, which prevents for using usual compactness arguments. For this reason,
747 we introduce a truncated version of the problem, which has also to be suitably regularized.
748 Let us denote by $\mathcal{T}_\Lambda^{R,\epsilon}$ the corresponding operator, where ϵ represents the regularization
749 parameter. This truncated and regularized operator appeared already in (32). Indeed, we
750 know from (32) that $\|\mathcal{T}_\Lambda^{R,\epsilon} - \mathcal{T}_\Lambda\| \rightarrow 0$ as $R \rightarrow \infty$ and $\epsilon \rightarrow 0$, hence, this implies
751 that $\|(\mathcal{T}_\Lambda^{R,\epsilon})^{-1} - (\mathcal{T}_\Lambda)^{-1}\| \rightarrow 0$ as $R \rightarrow \infty$ and $\epsilon \rightarrow 0$ by continuity of the map
752 $\Pi : \mathcal{T}_\Lambda \mapsto (\mathcal{T}_\Lambda)^{-1}$. Moreover, $(\mathcal{T}_\Lambda^{R,\epsilon})^{-1}$ is well-defined, continuous and compact, see
753 (32, Appendix. B). The discrete operators $(\mathcal{T}_\Lambda^I)^{-1}$ converge pointwise to $(\mathcal{T}_\Lambda^{R,\epsilon})^{-1}$, and the
754 compactness of $(\mathcal{T}_\Lambda^{R,\epsilon})^{-1}$ ensures that the discrete operator converges uniformly to $(\mathcal{T}_\Lambda^{R,\epsilon})^{-1}$,
755 for $0 < R < \epsilon$ and $0 < \epsilon < 1$ fixed (see (49) for more details on this fact). Following (49), we
756 deduce that the numerical eigenelements (λ^I, N^I) converges to $(\lambda^{R,\epsilon}, N^{R,\epsilon})$, the eigenelements
757 of $(\mathcal{T}_\Lambda^{R,\epsilon})^{-1}$, while preserving their algebraic multiplicity. Finally the uniform convergence
758 $\|(\mathcal{T}_\Lambda^{R,\epsilon})^{-1} - (\mathcal{T}_\Lambda)^{-1}\| \rightarrow 0$ as $R \rightarrow \infty$ and $\epsilon \rightarrow 0$ ensures the convergence of $(\lambda^{R,\epsilon}, N^{R,\epsilon})$
759 to (λ, N) , (32).

760 1.3 Numerical results

For some specific fragmentation kernels and growth rates, the eigenpair (λ, \bar{N}) is explicitly known, see (32). We can use these formula to check that the algorithm is able to find the expected values and profiles. To this end, we introduce the relative errors

$$E_\lambda^h = \frac{|\lambda - \tilde{\lambda}|}{\tilde{\lambda}} \quad \text{and} \quad E_V^h = h \sum_{i=1}^I |N_i^{(K)} - N(ih)|$$

761 where $N^{(K)}$ and N are both normalized by $h \sum_{i=1}^I N_i^{(K)} = h \sum_{i=1}^I N(ih) = 1$.
762

763 **Mitosis fragmentation kernel.** We start with the binary division kernel:

$$k(z|z') = \delta_{z'=2z}. \quad (22)$$

764 The associated division operator is described by (2). We assume that a and V are constant. In
765 this specific case the eigenpair is given by

$$\lambda = a, \quad N(z) = \bar{N} \sum_{n=0}^{\infty} (-1)^n \alpha_n \exp\left(-2^{n+1} \frac{a}{V} z\right), \quad (23)$$

with $\bar{N} > 0$ an appropriate normalizing constant and $(\alpha_n)_{n \in \mathbb{N}}$ is the sequence defined by the recursion

$$\alpha_0 = 1, \quad \alpha_n = \frac{2}{2^n - 1} \alpha_{n-1}.$$

766 In practice we shall use a truncated version of the series that defines N . For the numerical tests,
 767 we use the parameters collected in **Table 4**.

a	V	R	ϵ
4	0.6	5	10^{-6}

Table 4. Data for the numerical tests: binary division kernel

Number of cells	E_λ	E_V
1000	3.73×10^{-5}	3.83×10^{-2}
2000	5.68×10^{-8}	1.93×10^{-2}
4000	6.77×10^{-7}	9.69×10^{-3}
8000	6.84×10^{-7}	4.85×10^{-3}

Table 5. Binary division kernel: errors for several number of grid points

768 With this threshold ϵ , the approached eigenpair is reached in 43 iterations, independently of the
 769 size step. **Fig. 10** represents the evolution of the error E_V^h as a function of h in a log-log scale:
 770 $N^{(K)}$ approaches N at order 1. The rate improves when using a quadrature rule with a better
 771 accuracy. For this test, the approximation of the eigenvalue is already accurate with a coarse
 772 grid; it is simply driven by the threshold ϵ and E_L^h does not significantly change with h .
 773

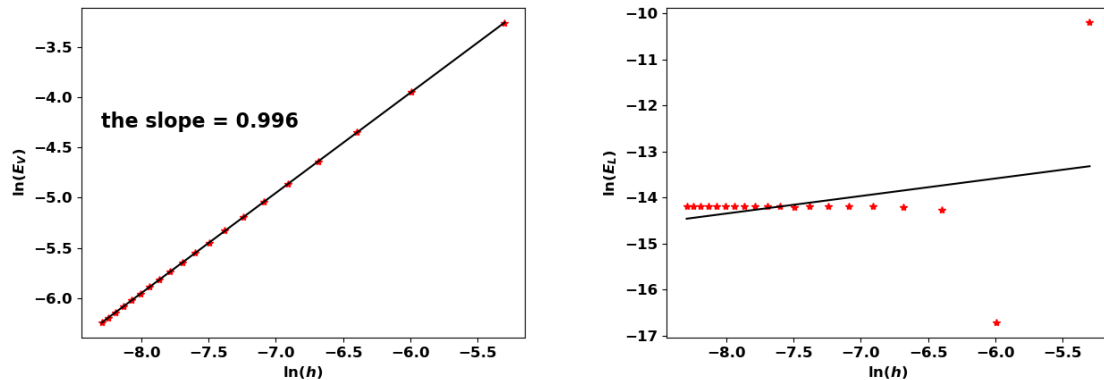


Figure 10. Binary division kernel: convergence rates of $(\lambda^{(K)}, N^{(K)})$ with respect to h

Uniform fragmentation. The uniform fragmentation kernel is defined by:

$$k(z|z') = \frac{1}{z'} \mathbf{1}_{0 \leq z \leq z'}.$$

774 We apply the algorithm for the following two cases:

1. $V(z) = V_0$ and $a(z) = a_0 z$. We have $\lambda = \sqrt{a_0 V_0}$ and

$$N(z) = 2\sqrt{\frac{a_0}{V_0}} \left(Z + \frac{Z^2}{2} \right) \exp \left(-Z - \frac{Z^2}{2} \right).$$

775 We still use the values in **Table 4** (especially, $a_0 = a$ and $V_0 = V$). The approximated
 776 eigenpair is obtained in 84 iterations and, as in the previous test, it does not change with the
 777 size step. In this case, both the eigenvalue and the eigenfunction are approached at order 1, see
 778 **Table 6** and **Fig. 11**.

Number of cells	E_λ	E_V
1000	1.30×10^{-2}	8.89×10^{-3}
2000	6.43×10^{-3}	4.50×10^{-3}
4000	3.23×10^{-3}	2.24×10^{-3}
8000	1.62×10^{-3}	1.13×10^{-3}

Table 6. Uniform fragmentation, ex. 1: errors for several number of grid points

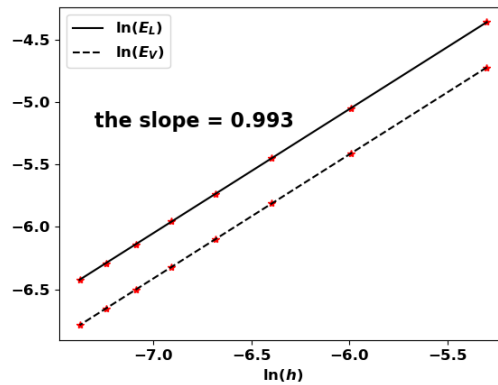


Figure 11. Uniform fragmentation, ex. 1: rate of convergence to the exact eigenpair with respect to h

779 2. $V(z) = V_0 z$ and $a(z) = a_0 z^n$ with $n \in \mathbb{N} \setminus \{0\}$. The eigenpair is defined by the following
 780 formula:

$n = 1$	$\lambda = V_0$	$N(z) = \frac{a_0}{V_0} \exp \left(-\frac{a_0}{V_0} z \right)$
$n = 2$	$\lambda = V_0$	$N(z) = \frac{2a_0}{\pi V_0} \exp \left(-\frac{a_0}{2V_0} z^2 \right)$
n	$\lambda = V_0$	$N(z) = \left(\frac{a_0}{nV_0} \right)^{\frac{1}{n}} \frac{n}{\Gamma(\frac{1}{n})} \exp \left(-\frac{a_0}{nV_0} z^n \right)$

782 Note that the growth rate V vanishes and Theorem 1.1 does not apply as such. Nonetheless,
 783 the algorithm works well and still captures the eigenpair. We perform the test for $n = 1$ and
 784 $n = 2$ and the results are recorded in **Table 7**, **Fig. 12** and **Table 8**, **Fig. 13**, respectively.

Number of cells	E_λ	E_V
1000	4.70×10^{-2}	2×10^{-2}
2000	2.43×10^{-2}	1.06×10^{-2}
4000	1.25×10^{-2}	5.5×10^{-3}
8000	6.39×10^{-3}	2.81×10^{-3}

Table 7. Uniform fragmentation, ex. 2, case $n = 1$: errors for different number of cells

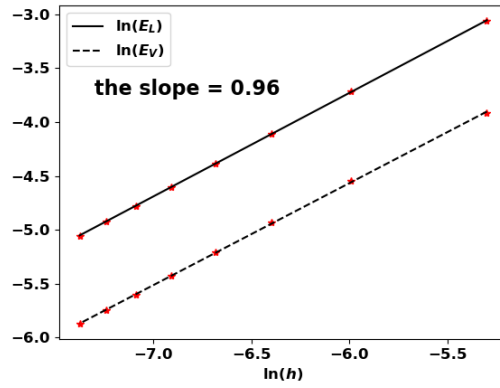


Figure 12. Uniform fragmentation, ex. 2 case $n = 1$: rate of convergence to the exact eigenpair with respect to h

Number of cells	E_λ	E_V
1000	2.39×10^{-2}	8.81×10^{-2}
2000	1.23×10^{-3}	4.53×10^{-3}
4000	6.41×10^{-3}	2.35×10^{-3}
8000	3.41×10^{-3}	1.24×10^{-3}

Table 8. Uniform fragmentation, ex. 2, case $n = 2$: errors for different number of cells

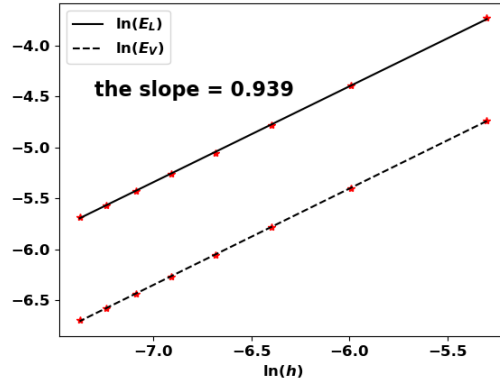


Figure 13. Uniform fragmentation, ex. 2: rate of convergence to the exact eigenpair with respect to h

2 SENSITIVITY ANALYSIS ON THE EQUILIBRIUM MASS

785 Having an efficient procedure to predict the residual mass of the equilibrium phase also opens
 786 perspectives to discuss the influence of the parameters. This can provide useful hints for the
 787 design and the optimization of anti-tumor therapies. We address this issue by performing a
 788 global sensitivity analysis on the immune-controlled tumor mass. Sensitivity analysis also
 789 provides information on the quantification of uncertainty in the model output with respect to the
 790 uncertainties in the input parameters. We remind the reader that the equilibrium mass is seen as a
 791 function of the parameters in **Table 1**:

$$\mu_1 = f(a, A, p, \chi, D, \gamma). \quad (24)$$

792 We consider that the input parameters are independent random variables uniformly distributed
 793 in an interval $[x_1, x_2] \subset (0, \infty)$:

$$M = (a, A, p, \chi, D, \gamma) \text{ with } M_i \sim U(x_1, x_2). \quad (25)$$

794 The pillar of the Sobol sensitivity analysis is the decomposition of f into $2^n - 1$ summands of
 795 increasing dimensions:

$$f(M) = f_0 + \sum_{i=1}^n f_i(M_i) + \sum_{1 \leq i < j \leq n} f_{ij}(M_i, M_j) + \cdots + f_{1 \dots n}(M_1, \dots, M_n), \quad (26)$$

796 where

$$\frac{1}{x_2 - x_1} \int_{[x_1, x_2]} f_{i_1 \dots i_p}(M_{i_1 \dots i_p}) dM_{i_k} = 0 \quad \text{for } k \in \{1, \dots, p\}, \quad (27)$$

797

$$f_0 = \frac{1}{(x_2 - x_1)^n} \int_{[x_1, x_2]^n} f(M) dM, \quad (28)$$

798

$$\int_{[x_1, x_2]^n} f_{i_1 \dots i_p}(M_{i_1 \dots i_p}) f_{j_1 \dots j_p}(M_{j_1 \dots j_p}) dM = 0, \quad (29)$$

799 and $M_{i_1 \dots i_p} = (M_{i_1}, \dots, M_{i_p})$. The existence and uniqueness of the above decomposition has
 800 been proven in (69), given f a square integrable function. Owing to the orthogonality condition
 801 (29), the total variance of f reads:

$$\mathcal{V} = \text{Var}(f(M)) = \frac{1}{(x_2 - x_1)^n} \int_{[x_1, x_2]^n} f(M)^2 dM - f_0^2. \quad (30)$$

802 Given (26), \mathcal{V} can be decomposed as follows:

$$\mathcal{V} = \sum_{i=1}^n \mathcal{V}_i + \sum_{1 \leq i < j \leq n} \mathcal{V}_{ij} + \dots + \mathcal{V}_{1 \dots n}, \quad (31)$$

803 where the terms $\mathcal{V}_{i_1 \dots i_p}$, called partial variances read:

$$\mathcal{V}_{i_1 \dots i_p} = \frac{1}{(x_2 - x_1)^n} \int_{[x_1, x_2]^n} f_{i_1 \dots i_p}^2 dM_{i_1} \dots dM_{i_p}. \quad (32)$$

804 Following the description in (69), the Sobol' sensitivity indices are defined as follows:

$$S_{i_1 \dots i_p} = \frac{\mathcal{V}_{i_1 \dots i_p}}{\mathcal{V}}. \quad (33)$$

805 They verify

$$\sum_{i=1}^n S_i + \sum_{1 \leq i < j \leq n} S_{ij} + \dots + S_{1 \dots n} = 1. \quad (34)$$

806 Each index $S_{i_1 \dots i_p}$ measures how the total variance of f is affected by uncertainties in the set of
 807 input parameters $i_1 \dots i_p$. An equivalent definition of the above indices is given by (see (68)):

$$\mathcal{V}_i = \text{Var}(\mathbb{E}(Y|M_i)), \quad \mathcal{V}_{ij} = \text{Var}(\mathbb{E}(Y|M_i, M_j)) - \mathcal{V}_i - \mathcal{V}_j, \dots \quad (35)$$

808 The total effect of a specific input parameter i is evaluated by the so-called total sensitivity index
 809 $S_T^{(i)}$, the sum of the sensitivity indices which contain i :

$$S_T^{(i)} = \sum_{C_i} S_{i_1 \dots i_p} \quad (36)$$

810 where $C_i = \{(i_1 \dots i_p) : \exists m \in \{1, \dots, p\}, i_m = i\}$. In practice, the sensitivity indices that
 811 are needed to discriminate the impact of the parameters are the first, second and total Sobol'
 812 sensitivity indices. The above indices are computed using Monte Carlo simulations combined
 813 with a careful sampling of the parameters space in order to reduce the computational load and
 814 the number of model evaluations. For this purpose, the following estimators can be derived
 815 using two different N samples A and B , see (68, 74),

$$\hat{f}_0 = \frac{1}{N} \sum_{l=1}^N f(M_l), \quad (37)$$

$$\hat{\mathcal{V}} = \frac{1}{N} \sum_{l=1}^N f^2(M_l) - \hat{f}_0^2, \quad (38)$$

816

$$\hat{\mathcal{V}}_i = \frac{1}{N} \sum_{l=1}^N f(M_{(-i)l}^{(A)}, M_{il}^{(A)}) f(M_{(-i)l}^{(B)}, M_{il}^{(A)}) - \hat{f}_0^2, \quad (39)$$

817

$$\begin{aligned} & \hat{\mathcal{V}}_{ij} \\ &= \frac{1}{N} \sum_{l=1}^N f(M_{-(i,j)l}^{(A)}, M_{il}^{(A)}, M_{jl}^{(A)}) f(M_{-(i,j)l}^{(B)}, M_{il}^{(A)}, M_{jl}^{(A)}) \\ & \quad - \hat{f}_0^2 - \hat{\mathcal{V}}_i - \hat{\mathcal{V}}_j. \end{aligned} \quad (40)$$

818 Here the notation $M_{-(i_1 \dots i_p)l}$ stands for the l -th sample line where we get rid of the points
819 corresponding to the indices i_1, \dots, i_p . The total sensitivity (87) is given by:

$$S_{T_i} = 1 - S_{-i} \quad (41)$$

820 where S_{-i} is the sum of all the sensitivity indices that do not contain the index i . Hence, the
821 total sensitivity index estimator reads:

$$\hat{S}_{T_i} = 1 - \frac{\hat{\mathcal{V}}_{-i}}{\hat{\mathcal{V}}} \quad (42)$$

where

$$\hat{\mathcal{V}}_{-i} = \frac{1}{N} \sum_{l=1}^N f(M_{(-i)l}^{(A)}, M_{il}^{(A)}) f(M_{(-i)l}^{(B)}, M_{il}^{(B)}) - \hat{f}_0^2.$$

REFERENCES

- 822 1 .Dunn GP, Bruce AT, Ikeda H, Old LJ, Schreiber RD. Cancer immunoediting: from
823 immunosurveillance to tumor escape. *Nat. Immunol.* **3** (2002) 991–998.
- 824 2 .Dunn GP, Old LJ, Schreiber RD. The immunobiology review of cancer immunosurveillance
825 and immunoediting. *Immunity* **21** (2004) 137–148.
- 826 3 .Koebel CM, Vermi W, Swann JB, Zerafa N, Rodig SJ, Old LJ, et al. Adaptive immunity
827 maintains occult cancer in an equilibrium state. *Nature* **450** (2007) 903–908.
- 828 4 .Boon T, Coulie PG, den Eynde BJV, van der Bruggen P. Human T -cell responses against
829 melanoma. *Annual Review of Immunology* **24** (2006) 175–208. doi:10.1146/annurev.
830 immunol.24.021605.090733. PMID: 16551247.
- 831 5 .Dranoff G. Cytokines in cancer pathogenesis and cancer therapy. *Nature Reviews Cancer* **4**
832 (2004) 11–22.
- 833 6 .Rabinovich GA, Gabrilovich D, Sotomayor EM. Immunosuppressive strategies that are
834 mediated by tumor cells. *Ann. Rev. Immunol.* **25** (2007) 267–296. doi:10.1146/annurev.
835 immunol.25.022106.141609. PMID: 17134371.
- 836 7 .Smyth MJ, Godfrey DI, Trapani JA. A fresh look at tumor immunosurveillance and
837 immunotherapy. *Nat. Immunol.* **2** (2001) 293–299. doi:10.1088/0031-9155/57/2/R1.

- 838 **8** .Whiteside TL. Immune suppression in cancer: Effects on immune cells, mechanisms
839 and future therapeutic intervention. *Seminars in Cancer Biology* **16** (2006) 3–15. doi:
840 <https://doi.org/10.1016/j.semcan.2005.07.008>. The Inflammation-Cancer Linkage: A
841 Double-Edged Sword?
- 842 **9** .Phan TG, Croucher PI. The dormant cancer cell life cycle. *Nature* **20** (2020) 398–411.
- 843 **10** .Atsou K, Anjuère F, Braud VM, Goudon T. A size and space structured model describing
844 interactions of tumor cells with immune cells reveals cancer persistent equilibrium states in
845 tumorigenesis. *J. Theor. Biol.* **490** (2020) 110163.
- 846 **11** .Kirschner DE, Panetta JC. Modeling immunotherapy of the tumor-immune interaction. *J.*
847 *Math. Biol.* **37** (1998) 235–252.
- 848 **12** .Konstorum A, Vella AT, Adler AJ, Laubenbacher RC. Addressing current challenges in
849 cancer immunotherapy with mathematical and computational modelling. *J. Royal Soc.*
850 *Interface* **14** (2017) # 20170150. doi:10.1098/rsif.2017.0150.
- 851 **13** .Lai X, Carson WE, Stiff A, Friedman A, Wesolowski R, Duggan M. Modeling combination
852 therapy for breast cancer with BET and immune checkpoint inhibitors. *Proc. Nat. Acad. Sc.*
853 **115** (2018) 5534–5539. doi:10.1073/pnas.1721559115.
- 854 **14** .de Pillis LG, Radunskaya AE, Wiseman CL. A validated mathematical model of cell-
855 mediated immune response to tumor growth. *Cancer Res.* **65** (2005) 7950–7958. doi:10.
856 1158/0008-5472.CAN-05-0564.
- 857 **15** .de Pillis L, Radunskaya A. The dynamics of an optimally controlled tumor model: A case
858 study. *Math. Comput. Modelling* **37** (2003) 1221–1244.
- 859 **16** .Kuznetsov V, Knott G. Modelling tumor regrowth and immunotherapy. *Math. Comput.*
860 *Modelling* **33** (2001) 1275–1287.
- 861 **17** .Li H, Wang S, Xu F. Dynamical analysis of tumor-immune-help T cells system. *Int. J.*
862 *Biomath.* **12** (2019) 1950075.
- 863 **18** .Robertson-Tessi M, El-Kareh A, Goriely A. A mathematical model of tumor–immune
864 interactions. *J. Theor. Biol.* **294** (2012) 56 – 73. doi:[https://doi.org/10.1016/j.jtbi.2011.10.](https://doi.org/10.1016/j.jtbi.2011.10.027)
865 027.
- 866 **19** .Wilkie KP, Hahnfeldt P. Modeling the dichotomy of the immune response to cancer: cytotoxic
867 effects and tumor-promoting inflammation. *Bull. Math. Biol.* **79** (2017) 1426–1448.
- 868 **20** .Chaplain MA, Kuznetsov VA, James ZH, Davidson F, Stepanova LA. Spatio-temporal
869 dynamics of the immune system response to cancer. Horn MA, Gieri S, Webb GF, editors,
870 *Mathematical models in medical and health science* (Vanderbilt University Press) (1998).
871 International Conference on Mathematical Models in Medical and Health Sciences.
- 872 **21** .Eftimie R. Investigation into the role of macrophages heterogeneity on solid tumour
873 aggregations. *Math. Biosc.* **322** (2020) 108325.
- 874 **22** .Kuznetsov VA, Makalkin IA, Taylor MA, Perelson AS. Nonlinear dynamics of immunogenic
875 tumors: Parameter estimation and global bifurcation analysis. *Bull. Math. Biol.* **56** (1994)
876 295–321. doi:10.1007/BF02460644.
- 877 **23** .Matzavinos A, Chaplain MAJ, Kuznetsov VA. Mathematical modelling of the spatio-
878 temporal response of cytotoxic *T*-lymphocytes to a solid tumour. *Math. Medicine and*
879 *Biology* **21** (2004) 1–34. doi:10.1093/imammb/21.1.1.
- 880 **24** .de Pillis LG, Mallet DG, Radunskaya AE. Spatial tumor-immune modeling. *Comput. Math.*
881 *Methods Medicine* **7** (2006) 159–176.

- 882 **25** .Eftimie R, Bramson JL, Earn DJD. Interactions between the immune system and cancer:
883 A brief review of non-spatial mathematical models. *Bull. Math. Biol.* **73** (2011) 2–32.
884 doi:10.1007/s11538-010-9526-3.
- 885 **26** .Eftimie R, Gillard JJ, Cantrell DA. Mathematical models for immunology: current state of
886 the art and future research directions. *Bull. Math. Biol.* **78** (2017) 2091–2134.
- 887 **27** .Eladdadi A, Kim P, Mallet D, editors. *Mathematical Models of Tumor-Immune System*
888 *Dynamics, Springer Proceedings in Math. & Statistics*, vol. 107 (Springer) (2014).
- 889 **28** .Mahlbacher GE, Reihmer KC, Frieboesa HB. Mathematical modeling of tumor-immune
890 cell interactions. *J Theor Biol.* **469** (2019) 47–60.
- 891 **29** .Roose T, Chapman SJ, Maini PK. Mathematical models of avascular tumor growth. *SIAM*
892 *Review* **49** (2007) 179–208.
- 893 **30** .Bellouquid A, Delitala M. Mathematical methods and tools of kinetic theory towards
894 modelling complex biological systems. *Math. Mod. Meth. Appl. Sci.* **15** (2005) 1639–1666.
- 895 **31** .Bekkal Brikci F, Clairambault J, Ribba B, Perthame B. An age-and-cyclin-structured cell
896 population model for healthy and tumoral tissues. *J. Math. Biol.* **57** (2008) 91–110.
- 897 **32** .Doumic-Jauffret M, Gabriel P. Eigenelements of a general aggregation-fragmentation model.
898 *Math. Models Methods Appl. Sci.* **20** (2010) 757–783. doi:10.1142/S021820251000443X.
- 899 **33** .Michel P, Mischler S, Perthame B. General relative entropy inequality: an illustration on
900 growth models. *J. Math. Pures et Appl.* **84** (2005) 1235–1260.
- 901 **34** .Michel P. Existence of a solution to the cell division eigenproblem. *Models Math. Meth.*
902 *App. Sci.* **16** (2006) 1125–1153.
- 903 **35** .Michel P. *Principe d'entropie généralisée et dynamique de populations structurées*. Ph.D.
904 thesis, Paris Dauphine (2005).
- 905 **36** .Perthame B. *Transport equations in biology*. Frontiers in Math. (Birkhauser) (2007).
- 906 **37** .Preziosi L. *Modeling Cancer Growth* (CRC-Press, Chapman Hall) (2003).
- 907 **38** .Alzahrani EO, Kuang Y. Nutrient limitations as an explanation of Gompertzian tumor
908 growth. *Disc. Cont. Dyn. Syst. B* **21** (2016) 357–372.
- 909 **39** .Gyllenberg M, Webb GF. A nonlinear structured population model of tumor growth with
910 quiescence. *J.Math. Biol.* **28** (1990) 671–694.
- 911 **40** .Iwata K, Kawasaki K, Shigesada N. A dynamical model for the growth and size distribution
912 of multiple metastatic tumors. *J. Theor. Biol.* **203** (2000) 177–186.
- 913 **41** .Benzekry S, Lamont C, Beheshti A, Tracz A, Ebos J, Hlatky L, et al. Classical mathematical
914 models for description and prediction of experimental tumor growth. *PLoS Computational*
915 *Biology* **10** (2014) e1003800. doi:10.1371/journal.pcbi.1003800.
- 916 **42** .Atsou K, Anjuère F, Braud VM, Goudon T. A size and space structured model of tumor
917 growth describes a key role for protumor immune cells in breaking equilibrium states in
918 tumorigenesis. *Plos One* (2021) 0259291.
- 919 **43** .Baccelli F, McDonald D, Reynier J. A mean field model for multiple TCP connections
920 through a buffer implementing RED. *Performance Evaluation* **49** (2002) 77–97.
- 921 **44** .Perthame B, Ryzhik L. Exponential decay for the fragmentation or cell-division equation. *J.*
922 *Differ. Eq.* **210** (2005) 155–177.
- 923 **45** .Faget J, Groeneveld S, Boivin G, Sankar M, Zangger N, Garcia M, et al. Neutrophils and
924 snail orchestrate the establishment of a pro-tumor microenvironment in lung cancer. *Cell*
925 *Report* **21** (2017) 3190–3204.

- 926 **46** .Li CY, Shan S, Huang Q, Braun RD, Lanzen J, Hu K, et al. Initial stages of tumor cell-
927 induced angiogenesis: evaluation via skin window chambers in rodent models. *J. Nat.*
928 *Cancer Institute* **92** (2000) 143–147. doi:10.1093/jnci/92.2.143.
- 929 **47** .Goudon T. *Mathematics for Modeling and Scientific Computing*. Mathematics and Statistics
930 (Wiley-ISTE) (2016).
- 931 **48** .Chatelin F. Convergence of approximation methods to compute eigenelements of linear
932 operations. *SIAM J. Numer. Anal.* **10** (1973) 939–948.
- 933 **49** .Chatelin F. The spectral approximation of linear operators with applications to the
934 computation of eigenelements of differential and integral operators. *SIAM Rev.* **23** (1981)
935 495–522.
- 936 **50** .Khou S, Popa A, Luci C, Bihl F, Meghraoui-Kheddar A, Bourdely P, et al. Tumor-associated
937 neutrophils dampen adaptive immunity and promote cutaneous squamous cell carcinoma
938 development. *Cancers* **10-12** (2020) E1860.
- 939 **51** .Farrell BE, Daniele RP, Lauffenburger DA. Quantitative relationships between single-cell
940 and cell-population model parameters for chemosensory migration responses of alveolar
941 macrophages to C5a. *Cell Motility* **16** (1990) 279–293. doi:10.1002/cm.970160407.
- 942 **52** .Friedman A, Hao W. The role of exosomes in pancreatic cancer microenvironment. *Bull.*
943 *Math. Biol.* **80** (2018) 1111–1133. doi:10.1007/s11538-017-0254-9.
- 944 **53** .Yates A, Callard R. Cell death and the maintenance of immunological memory. *Disc. Cont.*
945 *Dyn. Syst.-B* **1** (2001) 43–59. doi:10.3934/dcdsb.2001.1.43.
- 946 **54** .Beck RJ, Slagter M, Beltman JB. Contact-dependent killing by cytotoxic *T* lymphocytes
947 is insufficient for EL4 tumor regression in vivo. *Cancer Research* **79** (2019) 3406–3416.
948 doi:10.1158/0008-5472.CAN-18-3147.
- 949 **55** .Cazaux M, Grandjean CL, Lemaître F, Garcia Z, Beck RJ, Milo I, et al. Single-cell imaging
950 of CAR *T*-cell activity in vivo reveals extensive functional and anatomical heterogeneity. *J.*
951 *Experimental Medicine* **216** (2019) 1038–1049. doi:10.1084/jem.20182375.
- 952 **56** .Hanson HL, Donermeyer DL, Ikeda H, White JM, Shankaran V, Old LJ, et al. Eradication
953 of established tumors by *CD8+* *T*-cell adoptive immunotherapy. *Cell Press* **13** (2000)
954 265–276.
- 955 **57** .Nolz JC, Hill AB. Strength in numbers: Visualizing CTL-mediated killing in vivo. *Immunity*
956 **44** (2016) 207–208. doi:https://doi.org/10.1016/j.immuni.2016.01.026.
- 957 **58** .Kwok CS, Cole SE, Liao SK. Uptake kinetics of monoclonal antibodies by human malignant
958 melanoma multicell spheroids. *Cancer Res.* **48** (1988) 1856–1863.
- 959 **59** .Cairns CM, Gordon JR, Li F, Baca-Estrada ME, Moyana T, Xiang J. Lymphotactin
960 expression by engineered myeloma cells drives tumor regression: Mediation by *CD4+*
961 and *CD8+* *T*-cells and neutrophils expressing *XCR1* receptor. *J. Immun.* **167** (2001)
962 57–65. doi:10.4049/jimmunol.167.1.57.
- 963 **60** .Samson A, Lavielle M, Mentré F. Extension of the SAEM algorithm to left-censored data in
964 nonlinear mixed-effects model: Application to HIV dynamics model. *Comput. Stat. Data*
965 *Anal.* **51** (2006) 1562–1574. doi:10.1016/j.csda.2006.05.007.
- 966 **61** .[Dataset] Monolix version 2020R1. Antony, france: Lixoft sas (2020).
- 967 **62** .Weise K, Poßner L, Müller E, Gast R, Knösche TR. Pygpc: A sensitivity and uncertainty
968 analysis toolbox for Python. *SoftwareX* **11** (2020) 100450. doi:10.1016/j.softx.2020.100450.

- 969 **63** .Herman J, Usher W. SALib: An open-source Python library for sensitivity analysis. *The*
970 *Journal of Open Source Software* **2** (2017) joss00097. doi:10.21105/joss.00097.
- 971 **64** .Shashni B, Ariyasu S, Takeda R, Suzuki T, Shiina S, Akimoto K, et al. Size-based
972 differentiation of cancer and normal cells by a particle size analyzer assisted by a cell-
973 recognition pc software. *Biological and Pharmaceutical Bulletin* **41** (2018) 487–503.
974 doi:10.1248/bpb.b17-00776.
- 975 **65** .Moore GE, Sandberg AA, Watne AL. The comparative size and structure of tumor cells
976 and clumps in the blood, bone marrow, and tumor imprints. *Cancer* **13** (1960) 111–117.
977 doi:10.1002/1097-0142(196001/02)13:1<111::aid-cnrc2820130121>3.0.co;2-y.
- 978 **66** .Erdi YE. Limits of tumor detectability in nuclear medicine and PET. *Molecular imaging*
979 *and radionuclide therapy* **21** (2012) 23–28.
- 980 **67** .Harenberg D, Marelli S, Sudret B, Winschel V. Uncertainty quantification and global
981 sensitivity analysis for economic models. *Quantitative Economics* **10** (2019) 1–41. doi:10.
982 3982/qe866.
- 983 **68** .Saltelli A. Sensitivity analysis of model output. An investigation of new techniques.
984 *Computational Statistics and Data Analysis* **15** (1993) 211–238. doi:10.1016/0167-9473(93)
985 90193-W.
- 986 **69** .Sobol' I. Sensitivity estimates for nonlinear mathematical models. *Math. Modell. Comput.* **1**
987 (1993) 407–414.
- 988 **70** .Crestaux T, Le Maître O, Martinez JM. Polynomial chaos expansion for sensitivity analysis.
989 *Reliability Engineering and System Safety* **94** (2009) 1161–1172. doi:10.1016/j.ress.2008.
990 10.008.
- 991 **71** .Sudret B. Global sensitivity analysis using polynomial chaos expansions. *Reliability*
992 *Engineering and System Safety* **93** (2008) 964–979. doi:10.1016/j.ress.2007.04.002.
- 993 **72** .Ernst OG, Mugler A, Starkloff HJ, Ullmann E. On the convergence of generalized polynomial
994 chaos expansions. *ESAIM: Mathematical Modelling and Numerical Analysis* **46** (2012)
995 317–339. doi:10.1051/m2an/2011045.
- 996 **73** .Le Gratiet L, Marelli S, Sudret B. Metamodel-based sensitivity analysis: Polynomial chaos
997 expansions and gaussian processes. Ghanem R, Higdon D, Owhadi H, editors, *Handbook of*
998 *Uncertainty Quantification* (Cham: Springer International Publishing) (2017), 1289–1325.
999 doi:10.1007/978-3-319-12385-1_38.
- 1000 **74** .Saltelli A. Making best use of model evaluations to compute sensitivity indices. *Computer*
1001 *Physics Comm.* **145** (2002) 280 – 297. doi:https://doi.org/10.1016/S0010-4655(02)00280-1.
- 1002 **75** .Bailly C, Thuru X, Quesnel B. Combined cytotoxic chemotherapy and immunotherapy of
1003 cancer: modern times. *NAR Cancer* **2** (2020) 1–20.
- 1004 **76** .Galon J, Bruni D. Approaches to treat immune hot, altered and cold tumours with
1005 combination immunotherapies. *Nature Rev. Drug Discovery* **18** (2019) 197–218.
- 1006 **77** .Galon J, Costes A, Sanchez-Cabo F, Kirilovsky A, Mlecnik B, Lagorce-Pagès C, et al.
1007 Type, density, and location of immune cells within human colorectal tumors predict clinical
1008 outcome. *Science* **313** (2006) 1960–1964.
- 1009 **78** .Sharma P, Allison J. The future of immune checkpoint therapy. *Science* **348** (2015) 56–61.
- 1010 **79** .Champiat S, Tselikas L, Farhane S, Raoult T, Texier M, Lanoy E, et al. Intratumoral
1011 immunotherapy: from trial design to clinical practice. *Clin. Cancer Res.* (2020). doi:10.
1012 1158/1078-0432.CCR-20-0473.

- 1013 **80** .Kaufman HL, Atkins MB, Subedi P, Wu J, Chambers J, Mattingly TJ, et al. The
1014 promise of immuno-oncology: implications for defining the value of cancer treatment.
1015 *J. ImmunoTherapy of Cancer* **7** (2019) 129–140.
- 1016 **81** .Shekarian T, Valsesia-Wittmann S, Caux C, Marabelle A. Paradigm shift in oncology:
1017 targeting the immune system rather than cancer cells. *Mutagenesis* **30** (2015) 205–211.
- 1018 **82** .Wang H, Wang S, Huang M, Liang X, Tang Y, Tang Y. Targeting immune-mediated
1019 dormancy: a promising treatment of cancer. *Frontiers in Oncology* **9** (2019) 498:1–9.
- 1020 **83** .Correia AL, Guimaraes JC, der Maur PA, Silva DD, Trefny MP, Okamoto R, et al. Hepatic
1021 stellate cells suppress NK cell-sustained breast cancer dormancy. *Nature* **594** (2021) 566–
1022 592.
- 1023 **84** .Lopes N, Vivier E. Natural killer cells lull tumours into dormancy. *Nature* **594** (2021)
1024 501–502.
- 1025 **85** .Krein M, Rutman M. Linear operator leaving invariant a cone in a Banach space. *Amer.*
1026 *Math. Soc. Translation* **10** (1962) 199–325.
- 1027 **86** .Serre D. *Matrices: theory and applications, Graduate Texts in Math.*, vol. 216 (Springer)
1028 (2002).
- 1029 **87** .Homma T, Saltelli A. Importance measures in global sensitivity analysis of nonlinear
1030 models. *Reliability Engineering & System Safety* **52** (1996) 1 – 17. doi:[https://doi.org/10.](https://doi.org/10.1016/0951-8320(96)00002-6)
1031 [1016/0951-8320\(96\)00002-6](https://doi.org/10.1016/0951-8320(96)00002-6).